MODELLING OF CARDIOVASCULAR REGULATION IN HUMANS

MODELLING OF CARDIOVASCULAR REGULATION IN HUMANS

By

ANDREW MAY, B.SC.

A Thesis

Submitted to the School of Graduate Studies

in Partial Fulfillment of the Requirements

for the Degree

Master of Engineering

McMaster University

MASTER OF ENGINEERING (1998)
(Electrical and Computer Engineering)

McMaster University
Hamilton, Ontario

TITLE: Modelling of Cardiovascular Regulation in Humans

AUTHOR: Andrew May, B.Sc. University of Toronto

SUPERVISOR: Markad V. Kamath, Ph.D.

NUMBER OF PAGES: viii,94

Abstract

A linear state space model (LSSM) of cardiovascular regulation in ten normal human volunteers is developed using instantaneous lung volume (ILV), heart rate (HR), pulse pressure (PP) and mean arterial blood pressure (MBP) time series. Closed-loop transfer functions are computed and physiologically interpreted and the sensitivity of the transfer functions is assessed by comparison of supine and standing experimental results. The zeros of the transfer functions are used to infer the causality relationship between HR and PP. **Results** (1) In the supine condition, changes in ILV cause changes in HR within 0.5 s, followed shortly (0.3 - 0.5 s) by changes in PP and finally changes in MBP 1 - 2 s later. (2) When standing, changes in MBP occur concurrent with changes in PP. (3) MBP changes are dominated by blood pooling effects when standing. (4) Group delay is less affected than the magnitude by the physiological differences between the supine and standing conditions. (5) The relationship between HR and PP is neither completely causal nor anti-causal, but rather a combination of the two. (6) The minimum system delays are coincident with breathing frequencies between 0.2 - 0.4 Hz. **Conclusions** Closed-loop LSSM and transfer function analysis may be used to infer the time delays and causality of the closed-loop system response. The classical model of RSA generation is supported by the LSSM results.

Acknowledgments

Table of Contents

Table of Figures

Abbreviations

Abbreviation	Description
ABP	arterial blood pressure time series
AR	auto-regressive
ARMA	auto-regressive moving-average
AV	Atrio-Ventricular node
BP	blood pressure
ECG	electrocardiogram
FIR	finite impulse response
HF	high frequency (0.15 - 0.5 Hz)
HR	heart rate time series
HRV	heart rate variability
ILV	instantaneous lung volume time series
LF	low frequency (<0.15 Hz)
LSSM	linear state-space model
MBP	mean blood pressure time series
NARMA	non-linear auto-regressive moving average
$PaCO_2$	partial pressure of carbon dioxide
PaO_2	partial pressure of oxygen
PE	prediction error time series
PP	pulse pressure time series
PS/HRV	power spectral density analysis of heart rate variability
ROC	region of convergence
RSA	respiratory sinus arrythmia
SA	Sino-Atrial node
SIMO	single-input multiple-output
SISO	single-input single-output
S_{PE}	power spectral density of prediction error time series
SVD	singular value decomposition

Chapter 1: Introduction

1.1 Overview

In this thesis, instantaneous lung volume (ILV), heart rate (HR) and arterial blood pressure (ABP) time series are used to fit a single-input multiple-output (SIMO) linear state space model (LSSM) of cardiovascular regulation in healthy human volunteers. State space models are used extensively in the design of feedback control systems where it is necessary to control as well as predict the output of the system under investigation [Ljung 1987, Van de Vegte 1990]. The LSSM parameterization gives one easy access to the eigenvalues of the system under investigation. The eigenvalues are a useful estimate of the stability of the system and hence its sensitivity to noise and environmental conditions [Kailath 1980]. Thus, the LSSM is most useful for the simulation and control of mostly linear large-scale complex systems in industry, for example, where plant stability and controllability of the system outputs are major concerns.

The LSSM is mathematically equivalent to a generalized ARMA model, provided the AR and MA model orders are appropriately selected [Ljung 1990]. However, ARMA model order estimation is a difficult task in practice and the model coefficients may be

sensitive to uncertainty in the model order estimate [Banerjee 1996, Perrot 1996, Sinha 1983, Ljung 1987].

Unlike ARMA modelling techniques, the LSSM model order is estimated by comparing the rank of two data matrices using the singular value decomposition (SVD) [Moonen 1989, Golub 1996]. This vastly simplifies the order estimation procedure and results in a more robust model that is less sensitive to uncertainty in the order estimate [Moonen 1989]. Furthermore, the LSSM parameter estimation algorithm is linear, unlike ARMA models where the MA parameters must be estimated by non-linear iterative techniques [Ljung 1987]. Thus, the state-space approach may be considered to be an improved and yet simplified ARMA modelling technique.

In this thesis, the LSSM transfer functions are analytically derived from the model parameters and are physiologically interpreted. Since the transfer functions are parametric, they are not significantly influenced by additive noise in the input/output data, which is a large improvement over the FFT technique for transfer function estimation [Berger 1989, Saul 1991]. Like ARMA models, the LSSM parameters are computed simultaneously using all available data, so the LSSM transfer functions can accurately characterize the frequency response between all of the measured variables.

1.2 Neurophysiology of Cardiovascular Regulation [Berne 1990]

Cardiovascular regulation is the physiological process by which blood pressure (BP), gas concentrations and pH are varied to maintain physiological homeostasis. It is achieved through modulation of cardiac output, smooth muscle vascular tone and respiratory activity by both neurohormonal and central neurological control systems: the sympathetic and parasympathetic (or vagal). This thesis deals primarily with neural contributions to cardiovascular regulation.

1.2.1 Sympathetic Regulation

The sympathetic neural system is highly distributed and plays an important role in the regulation of three cardiovascular physiological functions: myocardial contractility, heart rate (HR) and vascular resistance. It consists of both afferent and efferent nervous limbs.

The afferent limb of the sympathetic system consists of both myelinated and unmyelinated nerve fibers. The afferent neurons have relatively high activation thresholds and the receptors are usually sensitive to only particular types of stimuli such as the local chemical environment (chemoreceptors) or mechanical distention (baroreceptors).

The efferent neurons originate primarily in the lower brain stem or along the spinal cord. A typical efferent activation pathway is shown in Figure 1. Preganglionic

sympathetic efferent neurons synapse to postganglionic neurons using nicotinic acetylcholine neurotransmitter. The postganglionic efferent fibers synapse to α and β-adrenergic receptors on smooth muscle and cardiac tissue. They release norepinephrine neurotransmitter when activated, however some sympathetic efferents (i.e. neurons responsible for regulation of sweat glands and vasodilatation of smooth muscle of vessels in skin and skeletal muscle) release muscarinic acetylcholine instead.

The adrenergic neurotransmitter released by activation of efferent sympathetic neurons is either carried away by the circulation or slowly reabsorbed by the efferent neuron. These processes are generally diffusion limited and hence sympathetic fiber deactivation is a relatively slow (3-7s) process [Berne 1990, Kamath 1993, Malik 1996, Malliani, 1992].

The release of epinephrine by sympathetic activation causes vasodilatation of capillaries at low concentrations (β-adrenergic effect) and vasoconstriction at higher concentrations (α-adrenergic effect). In all other vessels (arteries, arterioles, veins, etc.), sympathetic efferent activation causes vasoconstriction.

In many cases, the sympathetic response loops are positive feedback systems: Activation of a small population of sympathetic afferents often results in a response that tends to amplify the original afferent activity [Malliani 1992, Lown 1986]. These positive feedback control loops are counter-balanced by antagonistic activity of the parasympathetic (or vagal) neural subsystem, described in the following section.

1.2.2 Parasympathetic Regulation

Parasympathetic (or vagal) regulation differs from sympathetic regulation in several ways. The vagal innervation is less widely distributed than the sympathetic innervation and its effects are more local to the site of innervation. The afferent and efferent vagal branches penetrate further into the brain stem than the sympathetic neurons, with relatively fewer synapses in the spinal cord.

The typical vagal efferent activation pathway is shown in Figure 1. The main difference between the sympathetic and vagal reflex loops is that the vagal postganglionic efferent fibers have cholinergic receptors that are sensitive to muscarinic acetylcholine rather than norepinephrine. This neurotransmitter is rapidly hydrolyzed by acetylcholinesterase, especially near the sino-atrial (SA) and atrio-ventricular (AV) nodes of the heart. Thus, the effects of efferent vagal activation decay much faster (< 2 s) compared to sympathetic activation.
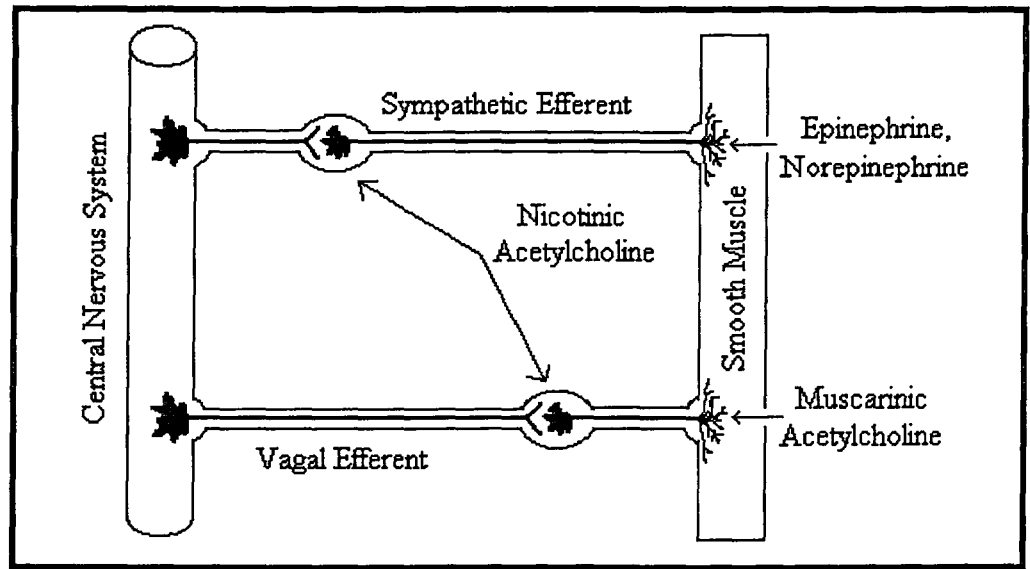
Figure 1: Efferent limb pathways of the sympathetic and vagal (parasympathetic) neural systems

1.2.3 Neural Modulation of Cardiac Activity

Vagal and sympathetic innervation of the heart are extensive. The sympathetic efferent innervation is widely distributed throughout the cardiac tissue but can be roughly separated into left and right branches. Most of the efferent fibers originate in the upper thoracic and cervical ganglia. Stimulation of the sympathetic efferent neurons to the heart increases the conduction velocity of cardiac electrical signals through the myocardium and reduces the diastolic depolarization time of the heart. This increases the instantaneous heart rate (HR) and the contractility of the cardiac tissue.

In the dog, stimulation of the left branch of efferent sympathetic fibers increases the left ventricular contractility, which leads to increased pulse pressure (PP). Stimulation

of the right branch increases both HR and contractility. The HR and contractility return to baseline values within 3-8 s following sympathetic efferent stimulation of the intact canine heart.

The vagal efferent cardiac innervation is more clustered than the sympathetic innervation, with most of the innervation near the AV and SA node. Most of the efferent fibers originate from the medulla oblongata in the brain stem.

Vagal and sympathetic efferent activity operate on the basis of *accentuated*[1] antagonism. Vagal activation causes inhibition of sympathetic efferent nerves and attenuates the response of cardiac tissue to the adrenergic compounds released by the sympathetic fibers, thereby reducing heart rate and decreasing cardiac tissue contractility. Stimulation of the left branch of the cardiac vagal efferents in the dog retards electrical conduction of the heart and may even stop propagation through the AV node (dromotropy). Stimulation of the right branch decreases the firing rate of the SA node (chronotropy) and hence decreases HR. The cholinergic neurotransmitters released by the vagal efferent fibers are quickly hydrolyzed by acetylcholinesterase contained in the SA and AV nodes. Thus, the effects of vagal activation are of short duration (0.5-2s).

---

[1] Accentuated antagonism implies that the effect of vagal activity on the end organ is approximately proportional to the amount sympathetic activity prior to vagal activation (and vice-versa). Hence, the vagal and sympathetic control mechanisms are mutually dependent.

1.2.4 Baroreceptor Reflex

The baroreceptors comprise several groups of predominantly vagal afferent neurons that are sensitive to mechanical distention in the blood vessels. The most important baroreceptors with respect to modulation of HRV are located in the aortic arch just outside the left ventricle and mainly in the carotid sinus at the bifurcation of the carotid artery in the neck. The firing rate of the receptors is proportional to the relative change in blood pressure in the artery. The carotid baroreceptors have highly adaptable thresholds. Thus, they are most sensitive when blood pressure changes rapidly. Abolishment of the pulse pressure via an external damping mechanism in the dog significantly reduces the carotid baroreceptor activity.

Increased activation of either set of baroreceptors in the dog causes an immediate activation of vagal cardiac efferents and concurrent withdrawal of sympathetic cardiac efferent activity. This results in decreased HR and myocardial contractility. Baroreceptor stimulation also modulates smooth muscle tone through sympathetic deactivation, which causes the arterioles and veins to dilate and hence lowers the blood pressure. This processes is associated with significant lag time (3-7 s) because of the longer lasting effects of adrenergic neurotransmitter release from the sympathetic neurons.

1.2.5 Bainbridge Reflex

A group of afferent vagal nerve fibers innervates the right atrium of the heart and is sensitive to atrial stretch or intravascular blood pressure. The neurons synapse in the medulla to vagal cardiac efferents forming the vagal-vagal reflex loop that is responsible for the Bainbridge reflex modulation of heart rate. The Bainbridge reflex causes the heart rate to increase whenever the preload pressure to the heart increases or the right atrium is otherwise distended (for example, during inspiration). The reflex is antagonistic to the baroreceptor reflex, as shown in Figure 2.
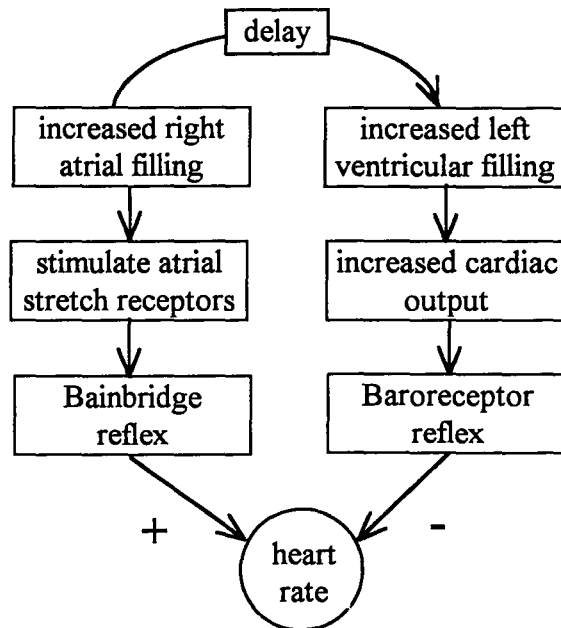
Figure 2: Antagonistic modulation of heart rate via the baroreceptor and Bainbridge reflex loops

1.2.6 Chemoreceptor Reflex

The chemoreceptors comprise a large set of central and peripheral afferent fibers originating in the medulla oblongata, in large vessel bifurcations throughout the cardiopulmonary vasculature and in the heart itself. The receptors are sensitive to the partial pressure of oxygen (PaO_2), carbon dioxide ($PaCO_2$) and pH of arterial blood. The main function of the chemoreceptors appears to be modulation of respiratory tidal volume and breathing frequency to maintain the concentration of blood gases and pH within physiological limits.

The PaO_2 carotid chemoreceptors are activated by a drop in PaO_2 in the arterial blood. The response to afferent stimulation is bimodal. Mild activation results in enhanced respiration concurrent with increased vagal activation in cardiac muscle and sympathetic activation in smooth muscle. This causes HR to decrease and preload blood pressure to the heart to increase. More intense afferent activation causes HR to increase rather than decrease.

The $PaCO_2$ receptors are activated by a rise in $PaCO_2$ in the arterial blood. Activation of the $PaCO_2$ chemoreceptors results in increased ventilation and breathing rate as well as vasoconstriction. The most important $PaCO_2$ receptors are distributed throughout the medulla oblongata and are associated with approximately 80% of $PaCO_2$ response. The remaining 20% of the $PaCO_2$ response is attributed to peripheral

chemoreceptors in the aortic and carotid arches. Activation of the peripheral $PaCO_2$ receptors decreases the left ventricular systolic pressure.

The pH chemoreceptors are located in the vasculature and the heart itself but not in the brain. The receptors are activated by a drop in arterial blood pH. The reflex response is increased ventilation and systemic vasoconstriction through sympathetic activation in smooth muscle.

1.2.7 Frank-Starling Effect

The cardiac muscle also responds to changes in loading conditions independent of autonomic modulation. Specifically, if the resting fill volume of the ventricles is increased by increased preload (venous) blood pressure then the subsequent ventricular contraction will be more forceful (Frank-Starling mechanism). This results in increased stroke volume and PP for the contraction. The Frank-Starling mechanism is intrinsic to the cardiac tissue itself but the response is modified by autonomic activity because neurotransmitters also modulate the contractility of the cardiac tissue.

1.3 Respiratory Sinus Arrhythmia (RSA)

A large component of HRV is associated with respiratory activity. This results in what is commonly called respiratory sinus arrhythmia (RSA) in HR and BP time series

[Berne 1990, Berger 1989, Bianchi 1997, DeBoer 1987, Freyschuss 1975, Kamath 1993, Malik 1996, Novak 1993, Piepoli 1997]. The arrhythmia has been studied extensively and is the physiological basis of the transfer function analysis of cardiovascular regulation presented in this thesis.

There are several physiological mechanisms that may potentially contribute to the generation of heart rate and blood pressure oscillations coincident with respiratory activity. The classical model of RSA is shown in Figure 3. In this model mechanical distention of the thoracic cage during inspiration imposes a positive pressure gradient on the venous return of blood to the heart thereby increasing blood flow to the lungs. The pressure gradient also activates vagal afferent stretch receptors in the right atrium which increases HR via the Bainbridge reflex. The enhanced blood flow propagates through the lungs and eventually (i.e. after a short time delay) raises the left ventricular filling volume, which results in increased stroke volume and PP via the Frank-Starling mechanism. The increase in PP is sensed by the aortic and carotid baroreceptors, which respond antagonistically by slowing HR through cardiac vagal activation and reducing arterial blood pressure via sympathetic deactivation in smooth muscle [Berne 1990]. Stretch receptors in the lungs are also believed to contribute to the response, although the nature of this contribution has proven to be difficult to characterize [Taha 1995, Freyschuss 1975]. Finally, a direct coupling between the medulla and the cardiac efferent nerves is also hypothesized to contribute or modulate RSA [Berne 1990]. The nature of this

coupling, if it exists, is topic of current research and considerable debate [Triedman 1994, Novak 1993, Piepoli 1997, DeBoer 1987].
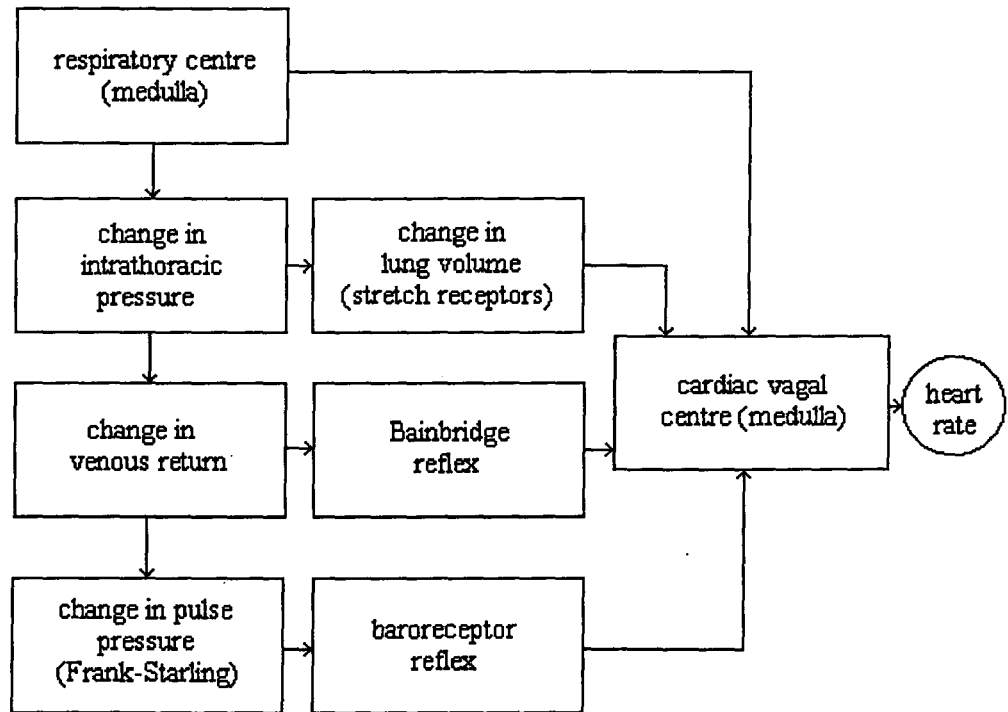
Figure 3 Classical model of RSA generation

1.3.1 Validation of the Classical Model of RSA

The contribution of the Frank-Starling mechanism to the classical model of RSA is supported by results in humans that show that HRV RSA is reduced but not abolished in heart and lung denervated patients [Bernardi 1989, Bernardi 1990, Taha 1995]. DeBoer et al. [1985] have fit a mathematical model of the known reflex components of the

classical RSA model using HR, BP and instantaneous lung volume (ILV) time series from normal humans with typical values for constants characterizing the baroreceptor and Bainbridge reflexes and Frank-Starling law of muscle fiber contraction. The model works surprisingly well, as evidenced by relatively low prediction error residuals, but other physiological data suggests that the simplified model may be inadequate because it does not describe all the relevant contributions to RSA. For example, single nerve recordings in the anesthetized dog show that sympathetic and vagal efferent nerve activities are also coupled to efferent phrenic nerve activity [Berne 1990]. The coupling to pherenic nerve activity persists even when respiratory motion is disabled and the blood is continuously oxygenated by an external system. Thus, in the dog, a component of RSA appears to be driven by intrinsic oscillations generated in the medulla.

This result is not supported by studies in humans which show that the RSA in human HRV is virtually abolished during short term voluntary apnea [Passino 1997]. This suggests that the central respiratory drive does not play a significant role in generation of RSA in humans. However, it is likely phrenic nerve activity is also suppressed during voluntary apnea. Thus, centrally generated respiratory rhythms may in fact contribute to RSA in humans under normal breathing conditions but may be inhibited during consciously controlled respiration or apnea.

A particularly insightful study [Taha 1995] has shown that the afferent innervation of lung also plays an essential role in generation of neurally mediated RSA in humans. They report that RSA is virtually abolished during controlled voluntary breathing in

patients with denervated lungs that have intact cardiac innervation and normal barorecptor gain. Large differences in HRV RSA magnitudes between the two groups suggests that the baroreceptor reflex may play an insignificant role in generation of RSA in humans. This is contrary to the explanation offered by the classical model of RSA generation and suggests that the classical model may not be entirely accurate.

However, other investigators have shown that RSA-type oscillations in HRV and PP in humans may be induced by suitable stimulation of carotid baroreceptors using an external neck suction device [Sleight 1995, Piepoli 1997]. Thus, in intact subjects the baroreflex may play an important role for the generation of HRV RSA but it appears that the baroreceptor mediated mechanisms may be disabled when lung afferents are severed.

Taha et al. [1995] also show that during positive pressure ventilation at a fixed frequency in normal conscious humans, the magnitude of the RSA drops dramatically compared to active (voluntary) controlled ventilation values. Since positive pressure ventilation does not result in atrial stretching (Bainbridge reflex) and suppresses normal phrenic nerve activity but not lung stretch afferent activation, they conclude that there are influences other than lung stretch afferents and the Bainbridge reflex responsible for the generation of RSA, but that the key mechanisms are not redundant and are, in fact, mutually dependent.

The exact physiological mechanisms responsible for the generation of RSA are still unclear. A number of investigators have suggested possible mechanisms and simple models but none have been able to fully integrate all the physiological results into a model

in which all plausible contributions are unambiguously characterized. Most physiological studies in RSA have been done either in anesthetized animals [Malliani 1992, Lown 1986, Berne 1990] or in humans with one or more of the regulatory systems disabled or otherwise controlled [Berger 1989, Bernardi 1989, Casadel 1992, Chon 1997, Freyschuss 1987, Jose 1966, Novak 1993, Passino 1997, Piepoli 1997, Sanders 1988, Saul 1991, Seals 1993, Taha 1995, Taylor 1995, Triedman 1994, Woo 1996]. These studies have provided critical information regarding the afferent and efferent components of cardiovascular regulation. However, little is known about how the various components interact under normal physiological conditions because it is difficult to record all of the relevant physiological signals *invivo* without surgical, pharmacological or mechanical intervention.

1.3.2 Effect of Controlled Breathing on RSA

The magnitude of the RSA in HRV depends on the state of the cardiac innervation, physiological state and breathing patterns. Actively controlled (voluntarily paced) respiration in humans partially overrides the normal respiratory control mechanisms and thus significantly changes the physiological state. This results in increased RSA in HRV and BP compared to spontaneous respiration with similar mean tidal volume and breathing rate. Previous investigators have shown that the magnitude of RSA in HRV during

controlled breathing is proportional to tidal volume and is inversely proportional to breathing rate [Taha 1995, Freyshuss 1975].

1.4 Closed-Loop Modelling of Cardiovascular Regulation

A number of investigators have used generalized linear and non-linear system identification approaches to model the physiological responses to controlled respiration in order to better characterize the closed-loop RSA response in humans [Saul 1991, Mullen 1997, Christini 1995, Chon 1997, De Boer 1987, Marmarelis 1993]. Generalized modelling techniques have allowed for accurate prediction of the normal physiological responses to controlled respiration. The main benefit of generalized modelling methods is that they have the potential to characterize the closed loop system response without making apriori assumptions regarding the underlying physiological components of the system that may contribute to the responses. The generalized model parameters can be used to better describe the integrated effect of the underlying physiological processes involved. Thus, it is hoped that models of the closed loop system characteristics may help fill the knowledge gap between the functional characteristics of the system components and the integrated response of the closed loop system.

The main disadvantage of the generalized modelling techniques is that the assumptions that must be made to fit the model (i.e. complete observability, identifiability, stationarity and often linearity) are usually rather poor assumptions when applied to

complex biological systems. Thus, the resulting models are often limited by uncertainty with respect to the reliability of the model and the subsequent interpretation of the model parameters in terms of plausible physiological mechanisms.

Previous investigators have used paced broad band breathing together with pharmacological interventions (Atropine and Propanalol) and changes in posture (standing and supine) to estimate non-parametric transfer functions between respiration, heart rate and blood pressure in healthy human subjects under two different physiological conditions [Saul 1991]. They found that between 0 - 0.5 Hz, vagal HR control (supine during adrenergic blockade with Propanalol) is characterized by a maximum gain near 0.15 Hz, a small decrease in gain with frequency above 0.15 Hz, and approximately 0° phase shift between ILV and HR. Under vagal blockade (standing with Propanalol), they found that HR control is characterized by lower gain at all frequencies with a phase shift that decreases from 180° at 0 Hz to -180° at 0.5 Hz. They also found that the ILV → PP and ILV → SBP magnitude functions were diminished but not abolished under total autonomic blockade (Propanalol + Atropine) and thus concluded that some, but not all blood pressure variablity is due to HRV.

Unfortunately, the set of transfer functions in [Saul 1991] are calculated using the fast Fourier transform (FFT) of the HR, ILV and BP time series taken two at a time. This technique is only reliable in feedforward systems where the input is strictly controlled [Saul 1991, Ljung 1987]. Thus, the output-output transfer functions (e.g. HR → PP) derived using the spectral methods are not reliable and cannot be used to characterize the

relationships between the system outputs even when this information is encoded in the input-output data.

The FFT technique is also very sensitive to noise in the measured data and windowing effects. Thus, the method requires relatively long data records to accurately estimate the transfer functions using ensemble averaging in the frequency domain. This is a disadvantage because it appears that the characteristics of cardiovascular regulation change continuously.

Finally, the non-parametric modelling technique used by [Saul 1991] has limited spectral resolution because the transfer functions are not parametric. This is a major disadvantage because one is then unable to reliably differentiate the phase function results to estimate the group delay of the system from the transfer function estimates. As it turns out, the group delay is an important parameter in transfer function interpretation and can be used to unambiguously infer the time delays of the system under investigation (see Section 1.6.4 for a detailed treatment of this topic). In [Saul, 1991] these time delays were incorrectly associated with the phase delays, leading to erroneous interpretation of the transfer function results. For example, in [Saul 1991] they observe that at most frequencies the vagal HR response to respiration "is characterized by a near zero by slightly positive phase". From this result, they erroneously conclude that "this implies that HR response actually leads the changes in ILV by a very small amount" when, in fact, it is the *slope* of the phase function (i.e. the group delay function) that defines this time delay.

More recently, other investigators have used similar experimental methods to calculate a specialized auto-regressive moving-average (ARMA) model of the cardiovascular regulation [Mullen 1997]. Unlike cross-spectral techniques, ARMA modelling facilitates characterization of all the output responses simultaneously during the parameter estimation. ARMA models can also separate the feedforward and feedback paths of a closed loop system more reliably than spectral models[2] [Ljung 1987]. The ARMA modeling technique is also less sensitive to noise and hence requires less input-output data to accurately fit the model parameters [Ljung 1987].

The ARMA model results in [Mullen, 1997] are presented as a group of impulse response functions that characterize the ILV → HR, ILV → ABP and ABP → HR transfer functions. Their results show that the ABP → HR impulse response decreases sharply at time t = 0 toward negative values. This reflects a very rapid decrease in HR in response to increased ABP, which they attribute to the baroreceptor reflex. They also find that HR rises in anticipation to corresponding changes in ILV, as shown by non-zero ILV → HR impulse response values for time t < 0. They claim that the non-causal ILV → HR impulse response supports the hypothesis that both HR and ILV and partially controlled by a common neural subsystem. Finally, they found that the ILV → ABP impulse response is characterized by a small decrease followed rapid increase in ABP. They explain the initial ABP decrease by the decrease the intrathoracic pressure upon inhalation.

---

[2] The reliability of the closed-loop ARMA models depends on the identifiability of the closed loop system. Unique parameterization of a closed loop system is often not possible, even when the system input is persistently exciting [Ljung 1987].

The subsequent increase is believed to be caused by increased cardiac filling after a 1-2 sec delay.

Unfortunately, the impulse response functions in [Mullen, 1997] are expressed exclusively in the time domain and hence do not facilitate interpretation of the frequency response of the system. This is a major limitation of the impulse response technique because oscillation appears to be a fundamental property of biological systems. The interpretation of the impulse responses in terms of physiological responses to respiration is also difficult to justify because normal respiration patterns do not resemble a train of impulses.

Mullen's decision to use a specialized ARMA model over the generalized model also introduces assumptions about the cardiovascular system that are not justifiable from the input-output data or known physiology. Specifically, in [Mullen 1997], the HR signal is assumed to vary discontinuously as a tachogram. The model structure also enforces causality on ILV → ABP and ABP → HR but not on ILV → HR, which is allowed to be non-causal. These assumptions make the physiological interpretation of the impulse response functions less reliable.

Other investigators have extended the ARMA modelling technique in [Mullen 1997] using a second order nonlinearity in order to calculate the two dimensional Volterra kernels as well as the system impulse responses [Marmarelis 1993, Chon 1997, Chon 1996]. Unfortunately, a detailed physiological interpretation of the non-linear parameters

was omitted. This may be because the physiological interpretation of parameters from generalized nonlinear models is a difficult task in practice.

1.5 Linear State-Space Models (LSSMs)

A generalized discrete time invariant LSSM may be written as

$$\underbrace{\vec{x}(k+1)}_{N\times 1} = \underbrace{A}_{N\times N}\underbrace{\vec{x}(k)}_{N\times 1} + \underbrace{B}_{N\times m}\underbrace{\vec{u}(k)}_{m\times 1} + \underbrace{\vec{w}(k)}_{N\times 1} \qquad (1)$$

$$\underbrace{\vec{y}(k)}_{n\times 1} = \underbrace{C}_{n\times N}\underbrace{\vec{x}(k)}_{N\times 1} + \underbrace{D}_{n\times m}\underbrace{\vec{u}(k)}_{m\times 1} + \underbrace{\vec{v}(k)}_{n\times 1}$$

Known Variables	Description
u(k)	k^{th} sample of input data where m is the number of inputs
y(k)	k^{th} sample of output data where n is the number of outputs

Unknown Variables	Description
x(0)	initial value of the N-element state-space vector
N	system order
A, B, C, D	state-space system matricies (time invarient)
w(k), v(k)	k^{th} sample of the state and measurement noise vectors

The state and measurement noise vectors, *w(k)* and *v(k)*, are not explicitly modelled by the LSSM algorithm used in this thesis but are assumed to contribute to the final prediction error of the model. Thus, no assumptions are made about the statistical properties of the noise signals except that they are not correlated with each other or the system inputs, outputs and states.

For the SIMO LSSM developed in this thesis, the input *u(k)* is the kth sample of the instantaneous lung volume (ILV) time series and the output *y(k)* is a 3 by 1 vector consisting of the kth sample of the instantaneous heart rate (HR), mean arterial blood pressure (MBP) and pulse pressure (PP) time series. The generation of these time series is described in Chapter 2. The system order, initial state vector, and system matricies may be estimated from the input-output data in four steps [Moonen 1989].

Step 1

Form a composite (block Hankel) data matrix using the 1st half of the input-output data

$$H = \begin{bmatrix} U \\ Y \end{bmatrix}_{(4i \times j)} \qquad (2)$$

where *U* and *Y* are block Hankel matrices of the input and output data respectively. For the LSSM models in this thesis *U* and *Y* are

$$U = \begin{bmatrix} ILV(1) & ILV(2) & \cdots & ILV(j) \\ ILV(2) & ILV(3) & \cdots & ILV(j+1) \\ \vdots & \vdots & & \vdots \\ ILV(i) & ILV(i+1) & \cdots & ILV(i+j-1) \end{bmatrix}_{(i \times j)} \qquad (3)$$

$$Y = \begin{bmatrix} HR(1) & HR(2) & \cdots & HR(j) \\ MBP(1) & MBP(2) & \cdots & MMBP(j) \\ PP(1) & PP(2) & \cdots & PP(j) \\ HR(2) & HR(3) & \cdots & HR(j+1) \\ MBP(2) & MBP(3) & \cdots & MBP(j+1) \\ PP(2) & BP(3) & \cdots & PP(j+1) \\ \vdots & \vdots & & \vdots \\ HR(i) & HR(2i+1) & \cdots & HR(i+j-1) \\ MBP(i) & MBP(2i+1) & \cdots & MBP(i+j-1) \\ PP(i) & PP(2i+1) & \cdots & PP(i+j-1) \end{bmatrix}_{(3i \times j)} \tag{4}$$

The choice of optimal values for i and j is discussed in Section 1.5.1.

Step 2

Calculate the singular value decomposition (SVD) of H and U.

$$H = U_H \bullet S_H \bullet V_H^T$$
$$U = U_U \bullet S_U \bullet V_U^T \tag{5}$$

The elements along the main diagonal of the S matricies are the singular values of U and H respectively [Golub 1996, Strang 1980]. The SVD of H has the useful property that the columns of V_H form an orthonormal basis for the rowspace of H, where the relative importance of each vector in V_H to the 'energy' in H is represented by the magnitude of the corresponding singular value in S_H. Thus, the vectors in V_H are the prinicipal components of the time series in H [Golub 1996].

If the input is sufficiently exciting and the system is linear and noise free (i.e. $w(k) = v(k) = 0$) then the rank of H will be greater than the rank of the U alone by an amount equal to the LSSM state space dimention [Moonen 1989].

$$Rank(H) = Rank(U) + N \qquad (6)$$

This allows one to estimate the system order, N, by visual comparison of the singular value plots of H and U prior to further computation of the model parameters, as illustrated in Figure 4.

Unlike ARMA modelling, the LSSM technique does not require the minimization of an information function applied to a set of hypothetical models to estimate the correct model order. This significantly reduces computation time while increasing the reliability of the order estimate [Moonen 1989].

Step 3

The first N principal components of H are the first N columns vectors in V_H. These vectors define an orthonormal basis for the intersection of the span of the input and output data spaces (i.e. the state-space), as shown in Figure 4. A valid realization of the state-vector sequence $x(k)$ may be found from any linear combination of these N principal vectors [Moonen 1989]. A particularly useful realization is

$$\vec{x}(k) = [\vec{x}_1(k)..\vec{x}_N(k)] = [V_{k1}, V_{k2},...,V_{kN}] \qquad (7)$$

where $x(k)$ is the state vector realization at discrete time k, V_{nm} is the $(n,m)^{th}$ element of V_H. In this case the state-space time series are mutually orthogonal. This corresponds to a minimal realization of (1), provided the system under investigation is completely controllable and observable [Kailath 1980, Moonen 1989].

In practice, noisy input-output data complicates the state vector reconstruction because noise increases the rank of H and U and hence introduces extraneous non-zero singular values into the S matricies. This makes it difficult to determine the correct system order from comparison of the singular value distributions of U and H. However, if the signal to noise ratio is large, the singular values introduced by the noise will all be smaller than smallest 'signal' singular values, as illustrated in Figure 4. This makes the singular value distribution discontinuous at the transition from the signal to noise subspaces. Moreover, using the first N principal components of H for the state-space reconstruction ensures that reconstruction is robust with respect to the model order estimation error. This is because the principal components are ordered with respect to their impotance in representing the time series in H [Golub 1996]. Thus, although the contribution of additive noise makes it difficult to place an exact *upper* limit on the system order, one is assured that the resulting system model still performs reasonably well.

Step 4

The matrices *A*, *B*, *C* and *D* are found by solving an over-determined set of linear equations in least squares

$$
\begin{bmatrix}
\vec{x}(2) & \cdots & \vec{x}(j) \\
HR(1) & \cdots & HR(j-1) \\
MBP(1) & \cdots & MBP(j-1) \\
PP(1) & \cdots & PP(j-1)
\end{bmatrix}
=
\begin{bmatrix}
A & B \\
C & D
\end{bmatrix}
\begin{bmatrix}
\vec{x}(1) & \cdots & \vec{x}(j-1) \\
ILV(1) & \cdots & ILV(j-1)
\end{bmatrix}
\quad (8)
$$

where *x(k)* is an *N* by 1 vector representing the kth sample of the state-space sequence found in Step 3.

A more efficient way to compute the LSSM matricies without explicit computation of *x(k)*, V_H, or the least squares solution of (8) is presented in [Moonen 1989]. The method is more computationally efficient and numerically robust but it is less intuitive than the proceedure described above. The improved algorithm in [Moonen, 1989] was rewritten as a MATLAB function for fitting the LSSMs presented in this thesis. An annotated version of this MATLAB implementation is included in Appendix A.
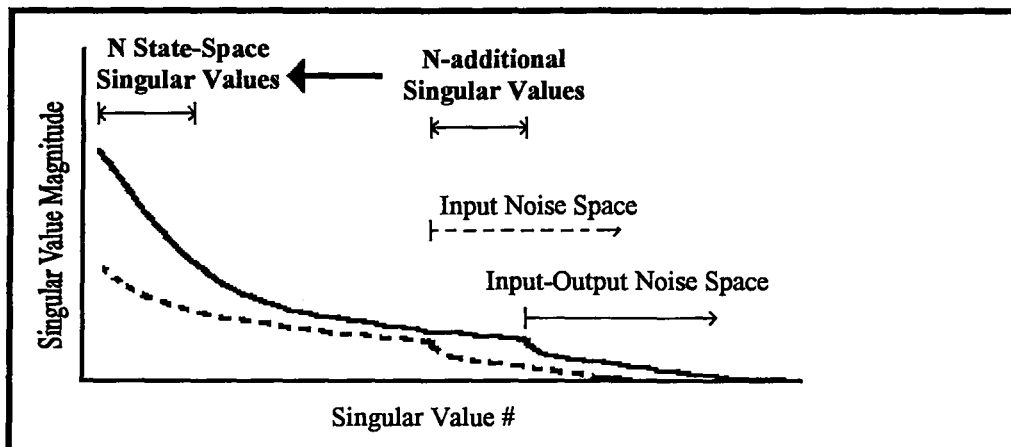
Figure 4: Determining a basis for the state-space. The dotted curve represents a typical singular value distribution for the input data matrix U. The solid curve is the distribution for the combined data matrix H. The output data adds N dimensions to U and the first N singular values in H form an orthonormal basis for the state space of the system.

1.5.1 Choosing the Data Matrix Dimensions

The rectangularity is defined as the ratio of the number of columns to the number of rows in the data matrix *H*.

$$R \equiv \frac{j}{i} \quad (9)$$

It should be selected empirically to maximize the number of columns in the data matrix subject to the constraint *Rank(H)* < *4i*, or more generally

$$Nullity(H^{T}) > 0 \quad (10)$$

This is done because the lowest frequency component that can be accurately estimated from the input-output data is limited by length of the rows in *H*. Thus, maximizing the number of columns is necessary in order to model the lowest frequencies possible, given a limited data set. At the same time, the accurate estimation of the system order requires that the singular value spectrum be distributed enough to accurately differentiate between eigenvectors associated with the signal and noise subspaces by visual inspection of the singular value spectrums of *H* and *U*. In practice, if the rectangularity is selected so that *Rowspace(H)* has only a few singular values that are very close to zero, then the spread of the singular value spectrum is maximized. This result follows from the general matrix property [Golub 1996]

$$Rank(H) = Rank(H^T) = \# \text{ of nonzero singular values in the SVD of H} \quad (11)$$

Thus, decreasing the matrix rectangularity beyond this point has no useful effect on the singular value distribution but unnecessarily increases the frequency of the minimum resolvable frequency component in the input-output data by reducing the length of each row in *H*.

1.6 Calculation of System Transfer Functions

A polynomial transfer function matrix $G(z)$ may be calculated from the LSSM matrices A, B, C and D [Kailath 1980]

$$G(z) = \frac{y(z)}{u(z)} = C(zI - A)^{-1}B + D \quad (12)$$

where I is an N by N identity matrix. This result is easily derived by taking the z-transform of the noise free version of (1) (i.e. $w(n) = v(n) = 0$) and solving for $y(z)/u(z)$. Note that for the (SIMO) case considered in this thesis, the elements of $G(z)$ are rational functions of the complex variable z where the ith row of $G(z)$ is the discrete time transfer function between the input and the ith output [Kailath 1980].

The transfer functions are found by evaluating the rows of $G(z)$ on the unit circle

$$z = \exp(j2\pi fT), \quad 0 \leq f \leq \frac{1}{2T} \quad (13)$$

where T is the sampling period of the input-output data in H and f is frequency in Hz. Since the LSSM is expressed in discrete time, the transfer functions are strictly bandlimited [Oppenheim 1989]. Note that the LSSM transfer functions are relatively noise free. This is because the system matrices are found from a least squares solution of the over-determined set of equations in (8).

1.6.1 Interpretation of Transfer Functions

The magnitude function

$$|G(f)| = \sqrt{\text{Re}\{G(f)\}^2 + \text{Im}\{G(f)\}^2} \qquad (14)$$

is the gain between the input (ILV) and the system outputs (HR, PP, and MBP) as a function of frequency [Oppenheim 1989].

The phase function

$$\Phi(f) = \arctan\left(\frac{\text{Im}\{G(f)\}}{\text{Re}\{G(f)\}}\right) \qquad (15)$$

is a measure of the distortion of the input signal (ILV) morphology as it passes through the system to the outputs. Phase distortion may take many different forms. In the simplest case, the phase shift will be constant with frequency. In this case a 90° phase shift indicates that the output is a frequency weighted function of the first derivative of the input, where the weighting function is the magnitude function (14). Similarly, a -90° phase shift function indicates an output dependence on the moving average or integral of the input function. Finally, a ±180° phase shift indicates that the input is inverted to produce the output [Oppenheim 1989, Van de Vegte 1990].

An arbitrary constant phase shift between ±180° indicates that the net response of the system output is a combination of the basic integral, derivative and inverter type responses. Clearly, the particular combination of the basic responses is not unique so even

with a perfectly constant phase function there is still ambiguity with respect to the underlaying physical mechanisms responsible for the phase response of the system. Note that the phase plot is cyclic with period 2π, so a phase shift exceeding $\pm180°$ is also ambiguous. This property introduces discontinuities in the phase function whenever the 'true' phase shift of the system exceeds $\pm180°$. The discontinuities in the phase function may be removed by 'unwrapping' the phase [Oppenheim 1989]. This implies adding multiples of $\pm\pi$ to the principal value phase function after a discontinuity.

Unwrapping the principal phase function (15) allows for net phase shifts in excess of $\pm180°$ and hence smooths out the appearance of the phase plot. However, phase unwrapping can only be accurately done in situations were the phase function is analytic. Specifically, with non-parametric techniques (e.g. [Saul, 1991]), noise in the phase function and limited spectral resolution may introduce anomalous discontinuities in the phase function that make it difficult or impossible to reliably unwrap the phase.

In addition to phase distortion information, the phase function also encodes the time delays of the system under investigation [Haykin 1989, Oppenheim 1989]. Extracting time delay information from the phase function is described in Section 1.6.4.

1.6.2 Determining Causality from Transfer Functions

It is often impossible to uniquely determine the relationship between the outputs of a multi-output system using only input-output data collected during closed-loop operation

[Ljung 1987]. This is because the relationship between the outputs of a closed loop system may be either causal, anti-causal, or neither [Oppenheim 1989]. For a SIMO system, determining the causality of the system outputs with respect to each other, if such a relationship exists, may require additional information or assumptions about the system that cannot be inferred from the input-output data alone [Ljung 1987, Oppenheim 1989, Kailath 1980].

In the simple case of a single-input single-output (SISO) system, causality implies that the output of the system is a function of only the past and present values of the input. Similarly, anti-causality implies that the output depends only on present and future values of the input. Specifically, if a SISO system is described by a transfer function $G(z)$, causality depends on the choice of the region of convergence (ROC) of $G(z)$, as illustrated in the following example (adapted from [Oppenheim1989, p 207]).

Example 1

Consider a linear time invariant system with input and output related through the difference equation

$$y[n] - \frac{5}{2}y[n-1] + y[n-2] = x[n]$$

The discrete time transfer function for this system is then

$$G(z) = \frac{1}{1 - \frac{5}{2}z^{-1} + z^{-2}} = \frac{1}{(1 - \frac{1}{2}z^{-1})(1 - 2z^{-1})}$$

The pole zero plot for *G(z)* is shown in Figure 5. There are three possible choices for the ROC. If the system is assumed to be causal, then the ROC is outside the outermost pole, i.e. $|z| > 2$. In this case, the system will not be stable since the ROC does not include the unit circle. If we assume the system is stable, then the ROC will be $1/2 < |z| < 2$. In this case, the system will be non-causal. For the third possible choice of ROC, $|z| < 1/2$, the system will be unstable and anti-causal.
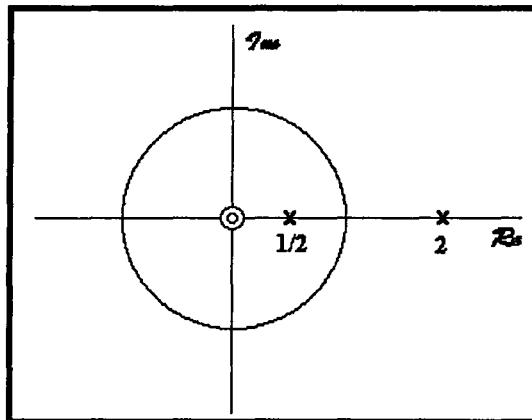
Figure 5 Zero-pole plot for Example 1.

Thus, if *G(z)* is such that the ROC is unknown and not unique, as in the above example, then one cannot make a definitive statement regarding the stability and causality of the physical system represented by *G(z)*. It is also clear that if *G(z)* is stable and has

poles both inside and outside the unit circle then the system is neither totally causal nor anti-causal but rather a combination of the two.

The determination of causality is further complicated by the fact that the inverse of a stable and causal system, $G^{-1}(z)$, may also be stable and causal, stable and non-causal, unstable and causal, or unstable and non-causal, depending on the locations of the zeros of $G(z)$ and the ROC. In general, $G(z)$ may be said to be *strictly* causal if and only if $G(z)$ is stable and causal and $G^{-1}(z)$ is stable and anti-causal. This is the only case in which one can conclude that the input must *drive* the output at all times. This result plays an important role in the analysis of causality for single-input multi-output (SIMO) systems like the one examined in this thesis.

1.6.3 Extracting Closed-Loop Transfer functions from the LSSM

The LSSM systems developed in this thesis may be decomposed into a set of global and local transfer functions shown in Figure 6. Here, the set of global transfer functions $\{G(z)\}$ are the rows of the $G(z)$ transfer function matrix in (12) obtained from the LSSM parameters as outlined in Section 1.6.
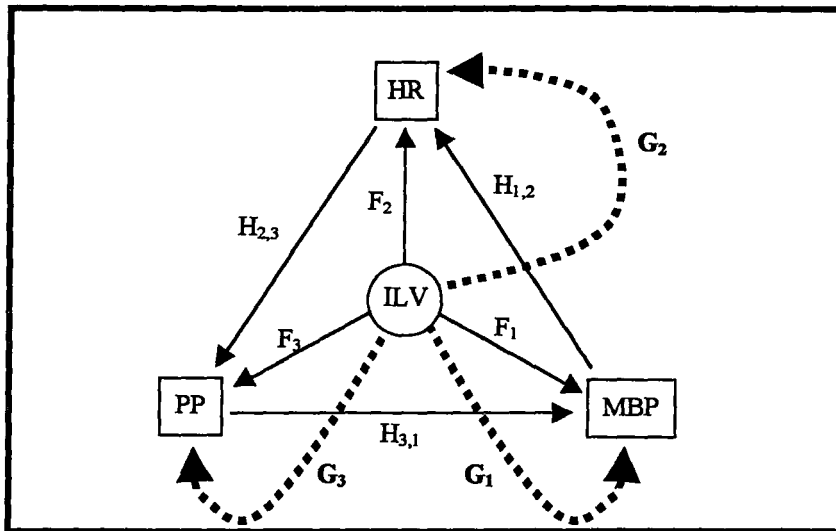
Figure 6 Schematic diagram of the system under investigation. The global transfer functions G_n may be derived from the LSSM parameters and (12).

Under certain conditions (see Appendix B for details), the set $\{H_{n,m}\}$ may be found from $\{G(z)\}$

$$H_{n,m}(z) \equiv \frac{y_n(z)}{y_m(z)} = \frac{G_n(z)}{G_m(z)} \qquad (16)$$

This simplifies to

$$H_{n,m}(z) = \frac{num\{G_n(z)\}}{num\{G_m(z)\}} \qquad (17)$$

where $num\{G_n(z)\}$ is the numerator polynomial of $G_n(z)$[3]. In this case, the poles of $H_{n,m}(z)$ are given by the zeros of $G_m(z)$. As shown in Appendix B, the $G_n(z)$ and $G_m(z)$ will have common zeros, in which case $H_{n,m}(z)$ will have multiple pole-zero cancellations. Clearly, only the poles and zeros that remain after cancellation are relevant to $H_{n,m}(z)$.

---

[3] This is because all the $G_n(z)$ share the common denominator $(zI-A)^{-1}$ from (12).

The global transfer functions *{G(z)}* are strictly causal because ILV is the control variable[4]. Similarly, the set *{F(z)}* is strictly causal even though *{F(z)}* is not known. However, the set of closed-loop transfer functions *{H(z)}* may or may not be causal because none of the outputs are explicitly controlled. From the results of Sections 2.4.2 and 2.4.3 one can conclude that $H_{n,m}(z)$ will be stable and strictly causal if and only if the all the zeros of $G_m(z)$ that are not common to $G_n(z)$ are contained *inside* the unit circle $|z| < 1$ and all the zeros of $G_n(z)$ that are not common to $G_m(z)$ are located *outside* the unit circle. If this is not the case then the closed loop causality is not clearly defined. For such systems, the group delay function plays an important role in clarifying the temporal relationships between the system outputs.

1.6.4 Interpretation of Group Delay

The group delay function

$$\Gamma_G(f) = -\frac{1}{2\pi}\frac{d\Phi(f)}{df} \qquad (18)$$

is the delay of the envelope of a narrow band ILV signal as it travels through the system [Oppenheim 1989, Haykin 1989]. A negative group delay over some frequency band $f_L < f < f_U$ means that the output changes are anticipatory to the input, provided the input

---

[4] Under normal physiological conditions respiration is controlled by the medulla, in which case causality of *G(z)* is no longer guarenteed. This is a limitation of the paced breathing method for system modelling.

signal is bandlimited to $f_L < f < f_U$ [5]. For example, if the input signal (ILV) is an amplitude modulated sinusoid[6]

$$ILV(t) \cong s(t)\cos(2\pi f_0 t) \qquad (19)$$

where $s(t)$ represents a slowly varying tidal volume[7] and f_o is the mean breathing frequency (assumed constant), then the output function $Y(t)$ will be [Haykin 1989, Oppenheim 1989]

$$Y(t) = s(t - \Gamma_G)\cos(2\pi f_0 t + \Phi(f_0)) \qquad (20)$$

Here, it is assumed that $|G(f)| = 1$ (unity gain at all frequencies) and that $\Gamma_G(f)$ is constant over the bandwidth of the ILV signal. Thus, if Γ_G is negative the output response to changes in tidal volume will *precede* the actual change in tidal volume by Γ_G seconds. This apparently non-causal behaviour is possible even in causal systems because narrow band signals are correlated in time and hence they are predictable given past values.

Note that the interpretation of the group delay is in the time domain. Thus, it is the group delay, *not* the phase delay, that defines the time delays of the system under investigation [Haykin 1989]. This is an important result that has been frequently

---

[5] In general, no real signal is strictly band-limited. This limits of the interpretation of group delay as the time delay of real signals through a system.

[6] This is a gross simplification of the true ILV signal properties but the results from this analysis may be extended to include any bandlimited ILV signal, which is a better approximation to the real ILV signal.

[7] Slow compared to the mean breathing frequency f_0

overlooked in the literature and has resulted in inaccurate physiological interpretation of

closed loop system transfer functions [Saul 1991, Berger 1989].

The group delay function is closely related to the magnitude function of $H(z)$

[Oppenheim 1989]. Specifically, a stable pole in the $H(z)$ will be respresented as a

positive spike in both (14) and (18) at the frequency of the pole. The magnitude of this

spike depends on the proximity of the pole to the unit circle ($|z| = 1$) and tends to inifinity

when the pole is located on the unit circle [Oppenheim 1989]. Similarly, a zero in the

transfer function will be represented as a negative spike in (14) at the frequency of the

zero and either a negative or positive spike in (18) depending on whether the zero is inside

or outside the unit circle respectively. As with the pole, the spike magnitude tends

towards $\pm \infty$ as the zero is moved towards the unit circle [Oppenheim 1989]. Thus,

strongly non-linear regions of the group delay functions are caused by poles or zeros that

are located close to the unit circle in the LSSM transfer functions. They have no simple

physical interpretation because the smallest *bandwidth* of the ILV signal is at least 0.05

Hz[8]. Unfortunately, large spikes in the transfer functions often interfere with the nearby

values of the magnitude and group delay functions near to the spike frequency, often

obscuring the more stable regions of these functions. One way to avoid this problem

would be to move all the poles and zeros of the system function away from the unit circle,

although this clearly would diminish the model accuracy and hence the validity of the

---

[8] This bandwidth limitation is based on the observation that one cannot generally predict the ILV time series further than 20s, or $\sim0.05^{-1}$ s into the future givin only past values of the ILV signal. In general, the predictability of a time series is inversely proportional its assumed bandwidth.

transfer functions. One may also pass the group delay function through a low pass filter to remove the spikes, but again, this would effect the reliablity of the group delay function.

Poles and zeros may be positioned close to the unit circle by the LSSM algorithm in order to model a strong resonance or damping in the system under investigation and/or by large amplitude intrinsic oscillations in the system outputs caused by unobservable system inputs. Both possibilities have the same effect on the transfer function and pole-zero plots of $G(z)$. However, if the source of the oscillation is an external input, then the prediction error power spectral density (PEP) of the model output will have a spike at the oscillation frequency, indicating a forced resonance phenomena where the forcing function is unknown and hence unpredictable beyond its second order statistics.

Chapter 2: Methods

2.1 Objectives

The main objective of this work is to develop a closed-loop model of cardiovascular regulation in humans and to interpret the model results in terms of normal physiology. In light of the previous work in this area, the secondary objectives of this work are (a) to refine the experimental and computational methodology used to generate the model, (b) to correct previous misinterpretations of transfer function results and (c) to investigate the theoretical limits and reliability of closed-loop system identification techniques.

2.2 Experimental Protocol

The experimental protocol was designed with three goals in mind: (a) to characterize the sensitivity of the LSSM technique to physiological changes caused by changes in posture (supine vs. standing), (b) to determine the reproducability of the LSSM results through repeated experiments with the physiological state held constant and (c) to

avoid any unneccassary physiological stresses or changes from the paced breathing requirements of the experiments.

Ten healthy, non-smoking human volunteers (6 male, 4 female, Age: 22-26 yrs.) participated in this study. No subject had a history of cardiopulmonary disease. All experiments were performed between 1 PM and 5 PM, 1-3 h after the last meal. Three different respiratory pacing waveforms with identical second order statistics (duration 300 s each) were generated in MATLAB by filtering 300 s white noise time series through a low pass digital filter (10th order FIR, 0.5 Hz cut-off). The pacing waveforms are shown in Figure 7. Twelve seconds of a sinusoidal breathing series (peak amplitude ½ maximum tidal volume, period 4 s) were smoothy attached to the start of the filtered noise series as a "lead-in" pacing series for the subjects. This ensured a smooth and reproducable transition between the physiological state associated with uncontrolled (spontaneous) breathing just before the experiment and controlled breathing during the experiment. Filtered white noise was used as the pacing signal so that the input to the system would be persistently exciting [Ljung 1987]. The cut-off frequency of the pacing waveforms was choosen to avoid undue physiological and mental strain from otherwise difficult or impossible breathing requirements. Three *different* waveforms were used to check the reproducability of the results from each subject and to avoid introducing a 'memory effect' into the results that may occur if the exact same waveform is used repeatedly in several consecutive trials on human subjects. The pacing waveforms were stored for visual playback using MATLAB on a personal computer (DELL XPS M200S).

During each of the experiments, one of the pacing waveforms was slowly scrolled across a computer screen, with 10 s of the waveform displayed on the screen at any point in time. An example of the pacing waveform display is shown in Figure 8. The subject was instructed to observe this waveform and modulate his instantaneous lung volume (ILV) according to a marker (a yellow dot) superimposed on the animated waveform, which indicated the current level of the pacing ILV signal. Since both current and future values of the pacing signal were visible during the waveform animation, the subject was able to accurately pace his lung volume without physiological or psychological stress from unpredictable breathing requirements.
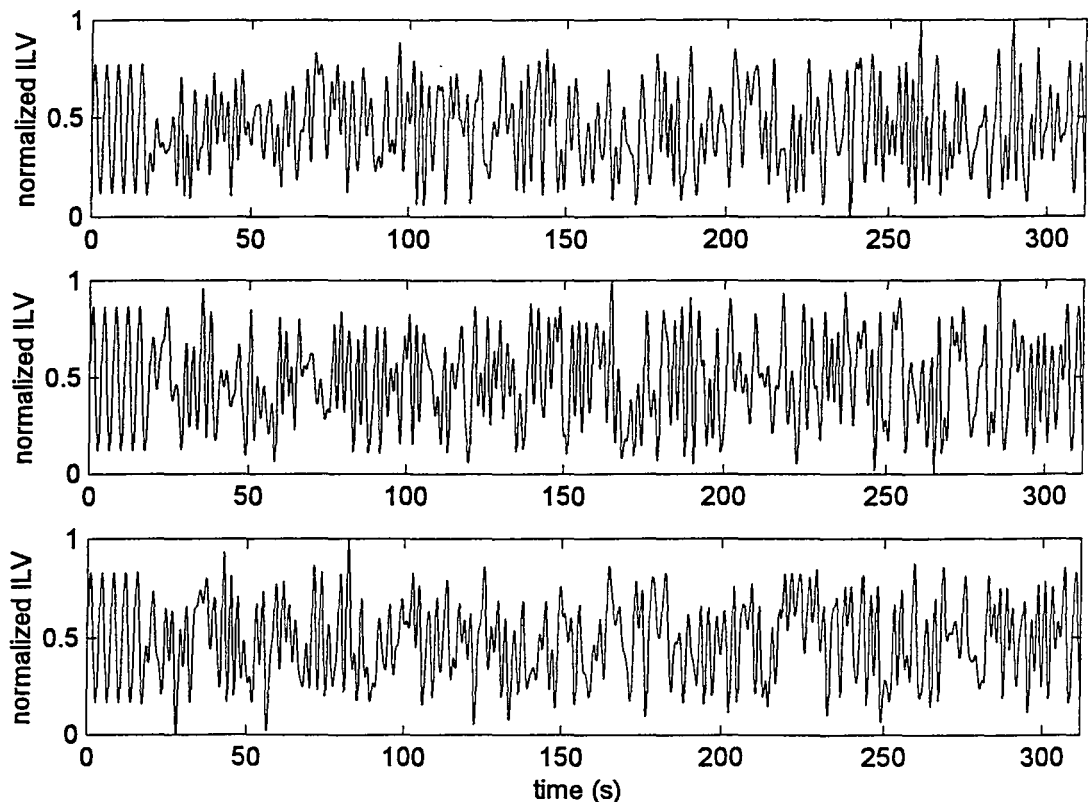
Figure 7: The three different ILV pacing waveforms used in this experiment. The physiological data was recorded immediately after the last cycle of the periodic 'lead-in' part of the pacing waveform.

The Lead II electrocardiogram (ECG, HP7807C amplifier), instantaneous lung volume (ILV, HP7807B chest-abdomen conductance plethysmography amplifier) and instantaneous arterial blood pressure (ABP, Ohmeda 2300 Finapres) were measured during each of the three paced breathing series (after the 12 s "lead-in" series) while supine. One to two minutes recovery time was allowed between the paced breathing experiments to ensure that initial physiological conditions were the same for each of the paced breathing series. The time series were sampled at 500 Hz with 12-bit resolution (DATAQ DI-420 data aquisition system) and stored on a personal computer for off-line analysis.

After the supine recordings, the subject was required to stand-up. Five minutes were allowed for the physiological state of the subject to stabilize. The three paced breathing experiments were then repeated in the standing condition for comparison.
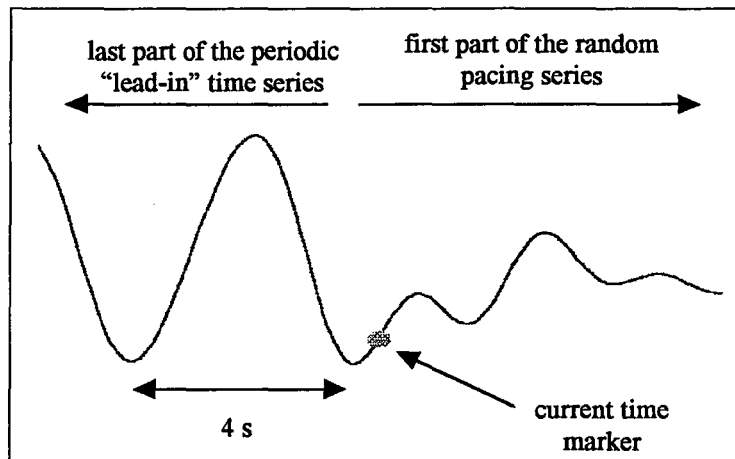
Figure 8 : An example of the respiration pacing waveform display. During the experiment, the waveform is animated and appears to move from right to left, with new pacing values appearing at the right edge of the screen. The current time marker moves up and down along the waveform but remains in the centre of the screen, indicating the current lung volume requirement to the subject.

2.3 Data Analysis

The recorded data were preprocessed using MATLAB to extract the relevant physiological information from the raw signals. Preprocessing is required to ensure that the input-output data can be linearly related and to remove components from the signals that might interfere with the LSSM algorithm. Thus, preprocessing removes some information from the input-output data (i.e. very low frequency baseline drift) but ensures that the remaining information can be accurately modelled.

2.3.1 Estimation of HR Time Series

The R-waves were detected from the ECG signal using a MATLAB peak detection algorithm developed in our laboratory [Kamath 1993]. A uniformly sampled HR time series was constructed at a sampling rate of 2 Hz using linear interpolation of the R-R intervals, as shown in Figure 9.

The interpolated HR series was high pass filtered (80th non-causal FIR filter with zero phase distortion) in order to remove frequency components < 0.07 Hz from the time series.

2.3.2 Estimation of MBP and PP Time Series

Mean blood pressure (MBP) and pulse blood pressure (PP) event series were formed using the mean ABP and the maximum change in ABP between each R-R interval from the ECG. The series were re-sampled at 2 Hz using linear interpolation of the event series with the R-R intervals from the ECG as the time reference, as shown in Figure 9. The interpolated MBP and PP were high pass filtered (80th order non-causal FIR filter with zero phase distortion) in order to remove frequency components < 0.07 Hz from the time series.

2.3.3 Synchronization of ILV Time Series

The ILV was low-pass filtered (10th order FIR linear phase, 1 Hz cutoff with delay compensation) and resampled at 2 Hz. The start and end times of the series were selected to coincide with the first and last R-waves in the ECG. This synchronized the HR and ILV time series to within ± 0.5 heart beats, on average.

Since the linear interpolation of the HR series is a non-causal process (see Section 5.6 for details), the ILV time series was advanced in time by 1 s prior to system identification in order to enforce causality on the input-output data. The effects of this artificial time lag were removed from the phase and group delay results after system

identification. The time-advanced ILV series was high pass filtered (80th non-causal FIR filter with zero phase distortion) in order to remove frequency components < 0.07 Hz from the time series.
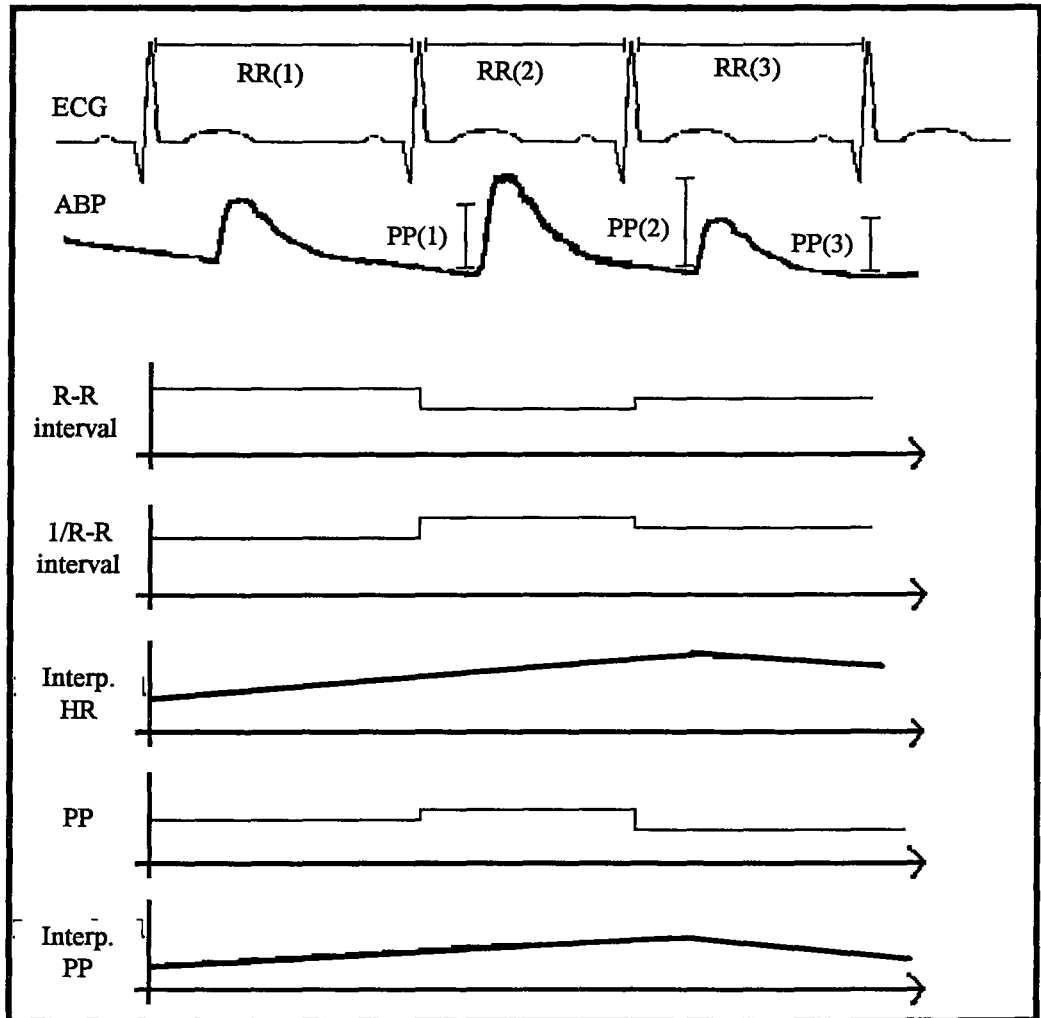
Figure 9 Conversion of HR and PP event series into interpolated discrete time series. ILV time series was synchronized with the interpolated HR, PP and MBP series by using the first and last R-waves to define the start and end times of the synchronized ILV time series.

2.4 Fitting the LSSM

A group of linear discrete time state-space models (LSSM) of cardiovascular regulation were estimated using the first 150 s of supine and standing data from each subject and the MATLAB algorithm in Appendix A. The rectangularity of the input-output data matrix was choosen to be 7, based on the theoretical results of Section 1.5.1. The rectangularity allowed for a maximum model order $N_{max} = 20$ with a minimum resolvable frequency component $F_{min} > 0.069$ Hz, or 10 cycles of a component with a period of 14.5 s, which is sufficient to accurately model the system at physiologically relevant breathing rates (0.07-0.5Hz).

The model order was between 15 - 18 and was selected by visual examination of the singular value distributions of the input and input-output data matrix of each set of results as outlined in Section 1.5.

Parametric transfer functions between ILV and HR, PP and MBP in each LSSM were computed using the method outlined in Section 1.6. The magnitude, phase and group delay functions were computed from the parametric transfer functions using the methods outline in Section 1.6.2. The poles and zeros of the HR $\rightarrow$ PP closed loop transfer function were derived from the ILV $\rightarrow$ HR and ILV $\rightarrow$ PP transfer functions using the results from Section 1.6.3 in order to investigate causality of the HR $\rightarrow$ PP response. The magnitude, phase and group delay of the closed loop transfer functions were computed

using the results of Sections 1.6 and 1.6.3, were the ROC is assumed to include the unit circle.

2.4.1 Model Validation

The models were validated using the remaining 150 s of data from each subject by comparing the measured system outputs (HR, BP and PP) with those predicted by the model given only the ILV signal as input. The prediction error (PE) was computed as the difference between the actual and predicted time series for each of the system outputs on the validation data. The auto and cross power spectral density functions for the prediction errors and ILV were estimated using the MATLAB functions psd() and csd() respectively, with 64 s data segments, overlapped by 50% and windowed with a Hamming window. The spectral resolution using these parameters was 0.03 Hz [MathWorks 1996, Ljung 1987]. The coherence function between the PE and ILV was computed from these spectral estimates using the relationship [Ljung 1987, Saul 1991]

$$\gamma^2(f) \equiv \frac{|S_{ILV,PE}(f)|^2}{S_{ILV}(f)S_{PE}(f)} \qquad (21)$$

where S_{ILV} and S_{PE} are the spectral density estimates of ILV and the PE respectively and $S_{ILV,PE}$ is the cross spectral density estimate.

Visual comparison of the predicted time series with the measured response was used as a qualitative measure of the model accuracy, which was checked by examination of the coherence between the ILV and PE. A significant coherence relationship ($\gamma^2 > 0.5$) between PE and ILV in regions of relatively large PEP was interpreted as poor model performance that could be caused either by a poor fit to the data or non-stationarity of the system being modelled.

Chapter 3: Results

3.1 Time Series

The interpolated time series from a typical subject in the standing condition are shown in Figure 10. In four of the ten subjects, MBP was observed to slowly decrease during the paced breathing by as much as 10 mmHg while HR slowly increased by up to 12 bpm. The MBP and HR returned back to their original mean values within 1-2 minutes of spontaneous breathing. Most of the subjects began to feel drowsy after the first or second paced breathing trials in the supine condition. The drowsiness persisted for several hours after the experiments were completed.
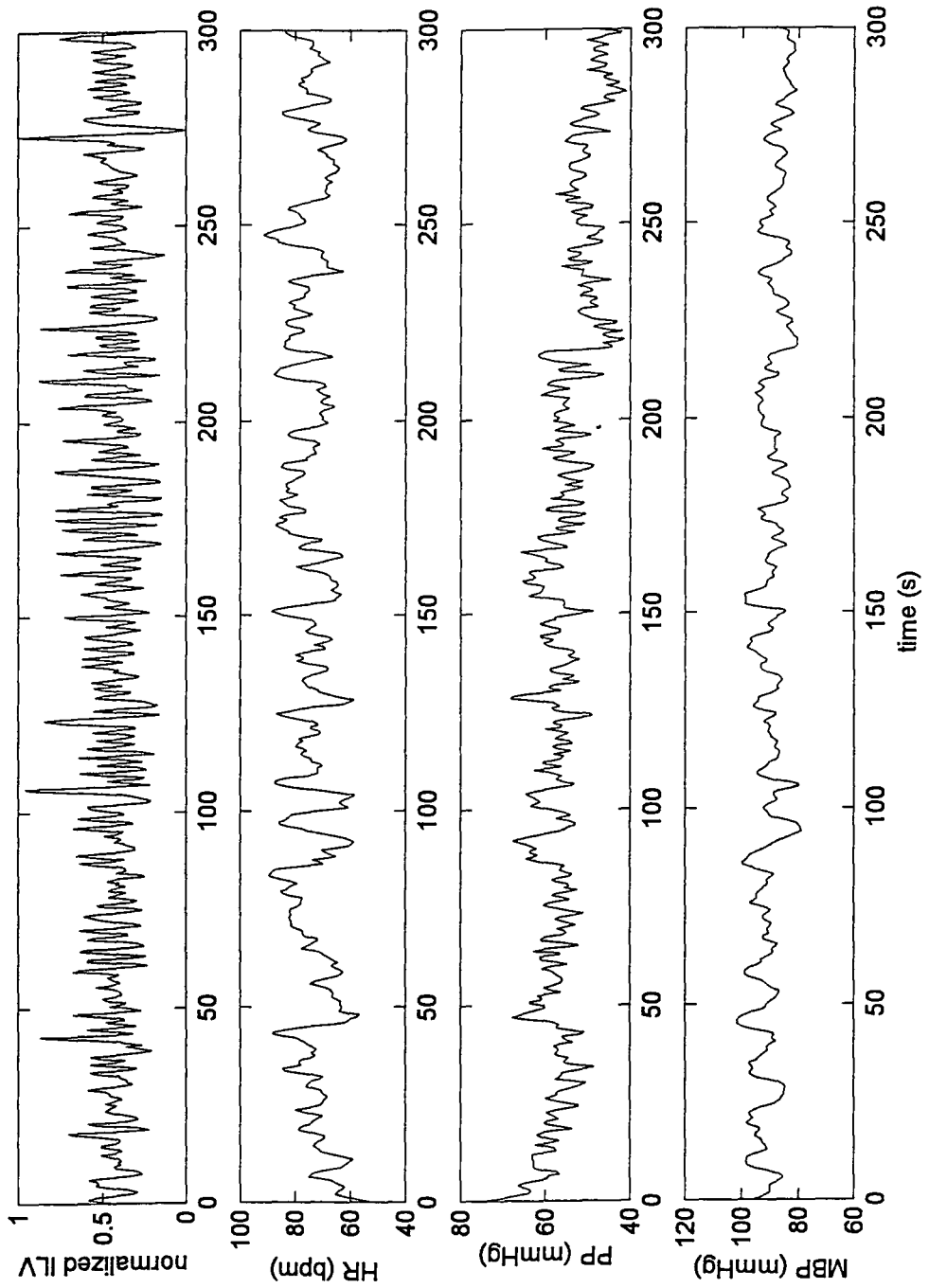
Figure 10 : Interpolated time series from a typical subject in the standing condition.

3.2 Simulations

The preprocessed HR, MBP and PP time series from a typical subject during paced breathing in the standing condition are shown in Figure 11(a). Superimposed on these plots are the predicted values for the time series, generated by passing the last 120 s of the ILV time series through the individual's LSSM. The simulations show that the LSSM captures most of the fast HR and PP variations associated with ILV. This is confirmed by the normalized prediction error power spectral density function (PEP) shown in Figure 11(b), which shows that PE is concentrated at low frequencies (<0.15 Hz). The coherence function in Figure 11(b) shows that the PE and ILV are not correlated wherever the PE power is significant, which confirms that the linear model has been fit correctly, even though the low frequency PEP is significant.
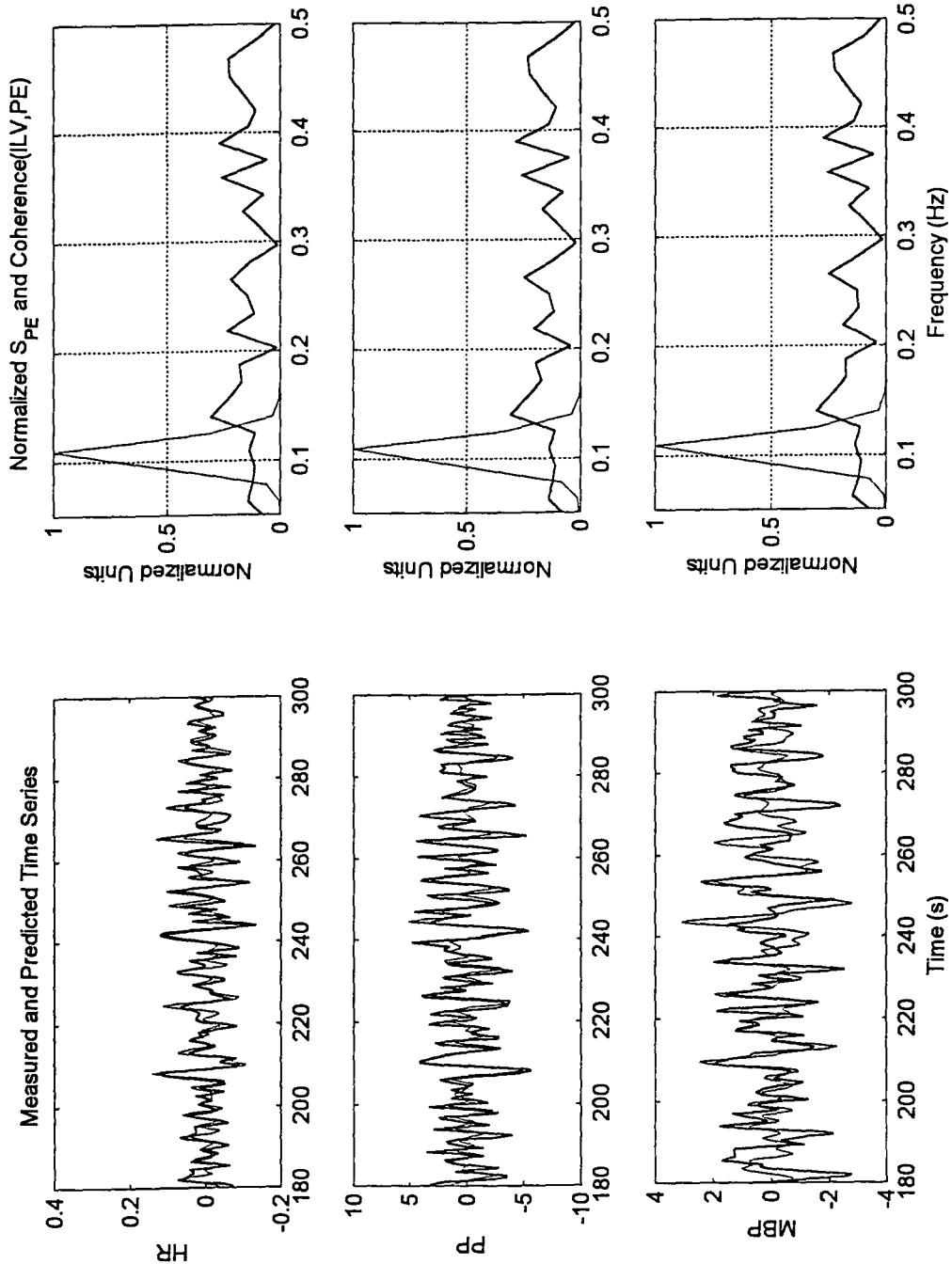
Figure 11 (a) Measured (heavy line) and predicted (light line) time series for a supine subject. The LSSM is able to capture much of the time series variability. (b) Corresponding prediction error power density spectrums (S_{PE}, thin line) and coherence function (heavy line) between ILV and PE. Prediction error power is concentrated at low frequencies (<0.15 Hz). Coherence function values are generally < 0.5 and indicate that the PE and ILV time series are not correlated, as expected.

3.3 Supine Transfer Functions

The combined set of supine transfer functions for the 10 subjects are shown in Figures 12 and 13. The inter-subject variability is high and there appears to be one outlier in the set with an abnormally large magnitude function. The common features of the supine state transfer function results are discussed below.

ILV→HR

The magnitude functions resemble a low pass filter with attenuation -16 ± 5 dB/decade. Thus, slow breathing has a markedly greater effect on HR than faster breathing. The phase functions generally decrease with frequency. A best fit line along the linear region of the phase functions yields a mean slope of -120° ± 60° per Hz or equivalently a mean group delay of about 0.3 - 0.6 s. If this linear trend is removed then the net phase shift is -30° ± 50° indicating that HR generally lags ILV by up to ¼ of the breathing cycle and that the particular response varies considerably with breathing frequency.

The group delay function has several spikes at the low frequency end (<0.15Hz) indicating a resonant phenomena in HR at low frequencies. The spikes tend to obscure any other

information contained in the group delay function except in the 0.2 - 0.4 Hz band, where the group delay is relatively stable at 0 ± 0.5 s.

ILV→PP

The ILV $\rightarrow$ PP magnitude functions resemble the ILV $\rightarrow$ HR magnitude functions. However the ILV $\rightarrow$ PP magnitude functions have a significantly higher attenuation constant (26 ± 8 dB / decade) which indicates a more rapid drop-off with frequency of the PP response to ILV.

The phase functions are relatively stable with a net phase of $\pm 180° \pm 30°$ and a linear trend of $-320° \pm 30°$ per Hz which yields a mean group delay of about 1 s or about twice the mean group delay of the ILV $\rightarrow$ HR results. The net phase shift indicates that PP changes oppose changes in ILV.

The group delay functions are scattered at low frequencies, again because of spikes in the group delay functions below 0.15 Hz. The function is relatively stable at frequencies >0.15Hz with a local minimum delay of 1 ± 0.5s around 0.3 Hz.

ILV → MBP

The attenuation constant of the magnitude functions is 11 ± 2 dB/decade, roughly in between the attenuation constants of PP and HR magnitude functions.

The phase functions generally decrease linearly with frequency with a net slope of -600° ± 180° per Hz, which yields about 1.6 - 2 s mean group delay. The detrended phase is relatively constant with frequency and has net phase shift of either 0° ± 30° (7 subjects) or ±200° ± 30° (3 subjects).

The local group delay functions vary significantly between subjects and therefore a detailed analysis of the system time delays between ILV and MBP is not feasible.

HR → PP

The magnitude functions are essentially constant with frequency. The variance of the magnitude function is greater than expected, probably because the large number of near pole-zero cancellations in the closed-loop transfer functions makes the computation of the HR → PP magnitude function numerically unstable. The phase and group delay functions are less affected by this problem. The best fit line to the phase function has a mean positive slope -180° ± 30° per Hz or a mean group delay of about 0.5 ± 0.2s s. The mean group delay is reflected in the local group delay function, which is stable between 0.15 - 0.4 Hz. Thus HR generally leads PP by about 0.5 s when supine. This implies that the time delay between ILV and PP is actually caused by a time delay between HR and PP.

HR → MBP

The magnitude function results are quite similar to the ILV → MBP transfer function except that the gain function is flatter and the mean slope of the phase function is reduced to approximately -360° ± 60° per Hz or about 0.8 - 1.2 s. Thus, part of the delay between ILV and MBP (1.5 - 2 s) may be attributed to a delay between HR and MBP.
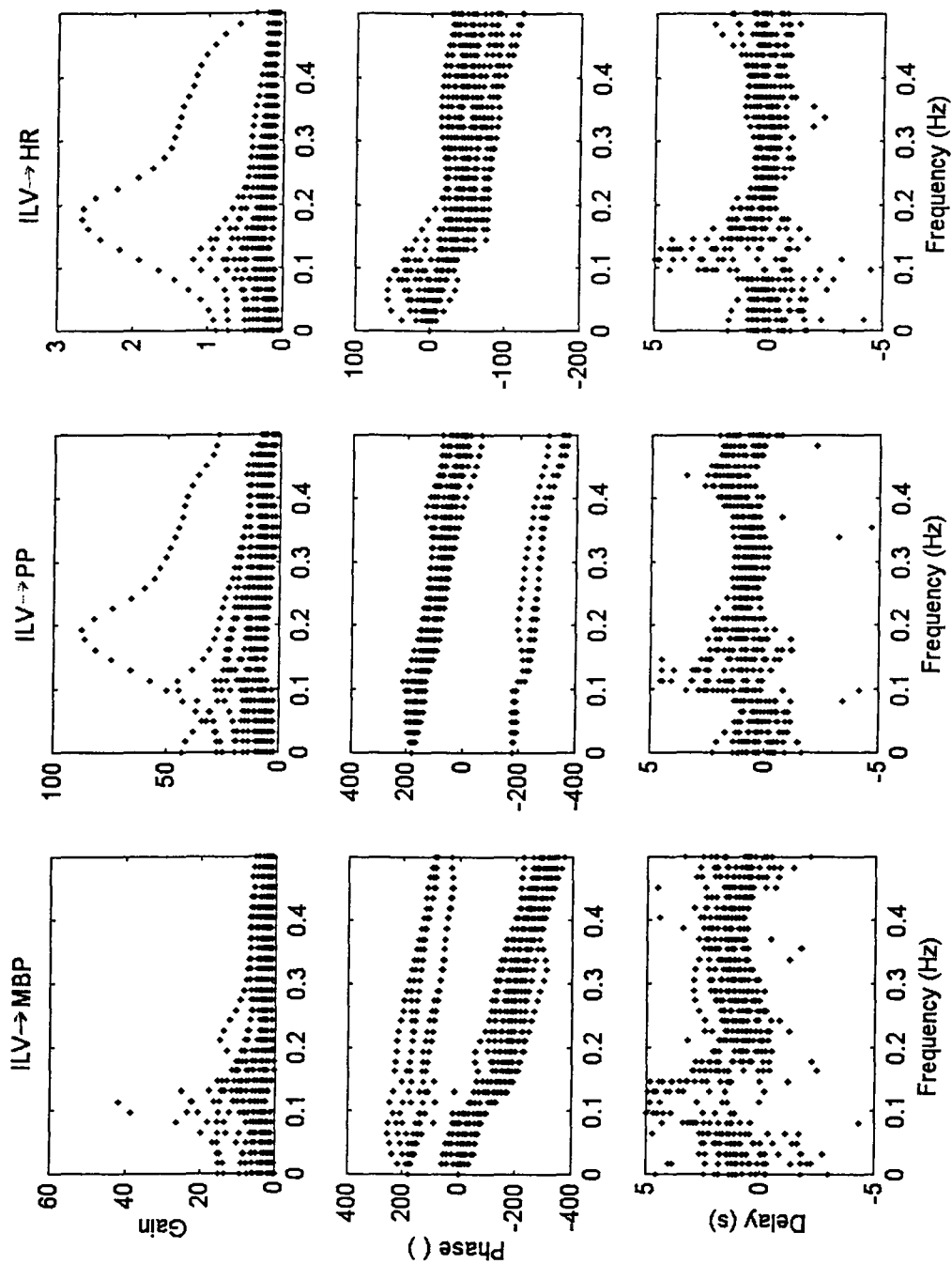
Figure 12: LSSM transfer functions for 10 subjects in the supine condition
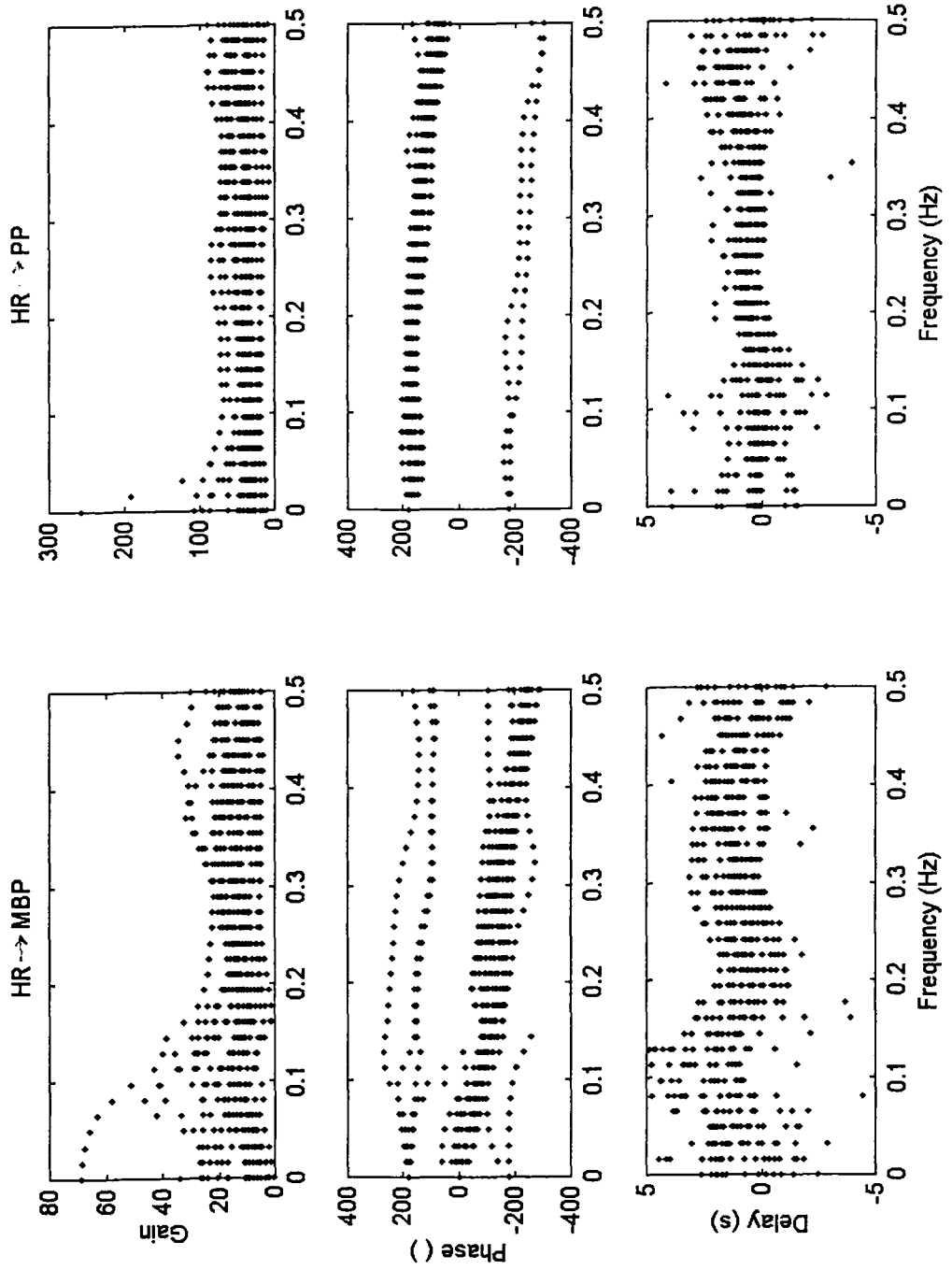
Figure 13 : LSSM closed-loop transfer functions for 10 subjects in the supine condition

3.4 Changes on Standing

The transfer function results from the ten subjects in the standing condition are shown in Figures 14 and 15. The results are mostly similar to the supine model results. The differences between the transfer function results are described below.

ILV → HR

The magnitude functions are attenuated by approximately 50% on standing with the attenuation constant relatively unchanged (17 ± 5 dB/decade compared to 16 ± 5 dB/decade). The phase functions become flatter with essentially zero slope and mean phase of $-50° \pm 60°$ between 0.1 - 0.5 Hz. Thus the HR response to ILV becomes more dependent on the integral of ILV than the derivative when standing.

The group delay functions are essentially unchanged by standing. The value of the group delay function at the local minimum appears slightly reduced although the change is not statistically significant.

ILV → PP

The ILV → PP magnitude functions are essentially unchanged upon standing with the exception of the attenuation constant which decreases from 26 ± 8 dB / decade to $14 \pm$

2 dB when standing. This indicates that PP response becomes less dependent on breathing frequency when standing but the peak magnitude of the response is relatively unchanged.

The phase functions are unchanged upon standing, with PP 180° ± 30° out of phase and delayed by about 1 s (phase slope -360° ± 50° per Hz). The group delay function is also essentially unchanged upon standing.

ILV → MBP

The ILV → MBP magnitude function is amplified by about 50% upon standing with a comparable increase in the attenuation constant from 11 ± 2 dB/decade to 24 ± 5 dB/decade. The phase function has a detrended net phase shift of ±180° ± 30° and the slope of the best fit line is reduced to -180° ± 30° per Hz which yields significantly smaller mean group delay of about 0.5 s, compared to 1.5 - 2s when supine.

The group delay function is much less variable for the standing transfer function results and exhibits the same morphology as the group delay functions for the HR and PP transfer functions. The local minimum in the group MBP group delay is 0 ± 1.5 s at 0.25 Hz.

HR → PP

As with the supine closed-loop transfer function, the HR → PP magnitude functions are affected by numerical stability problems because of multiple pole-zero cancellations, although the problem appears to be worse in the standing condition results. This makes it difficult to reliably interpret the magnitude function results. The phase and group delay functions, however, are less affected by this problem and are essentially unchanged upon standing.

HR → MBP

As the HR → PP results, the HR → MBP magnitude functions are numerically unstable. The net phase shift is unchanged upon standing (±180° ±30°) but the mean group delay is decreased from 1 ±1 s to 0 ±1 s.
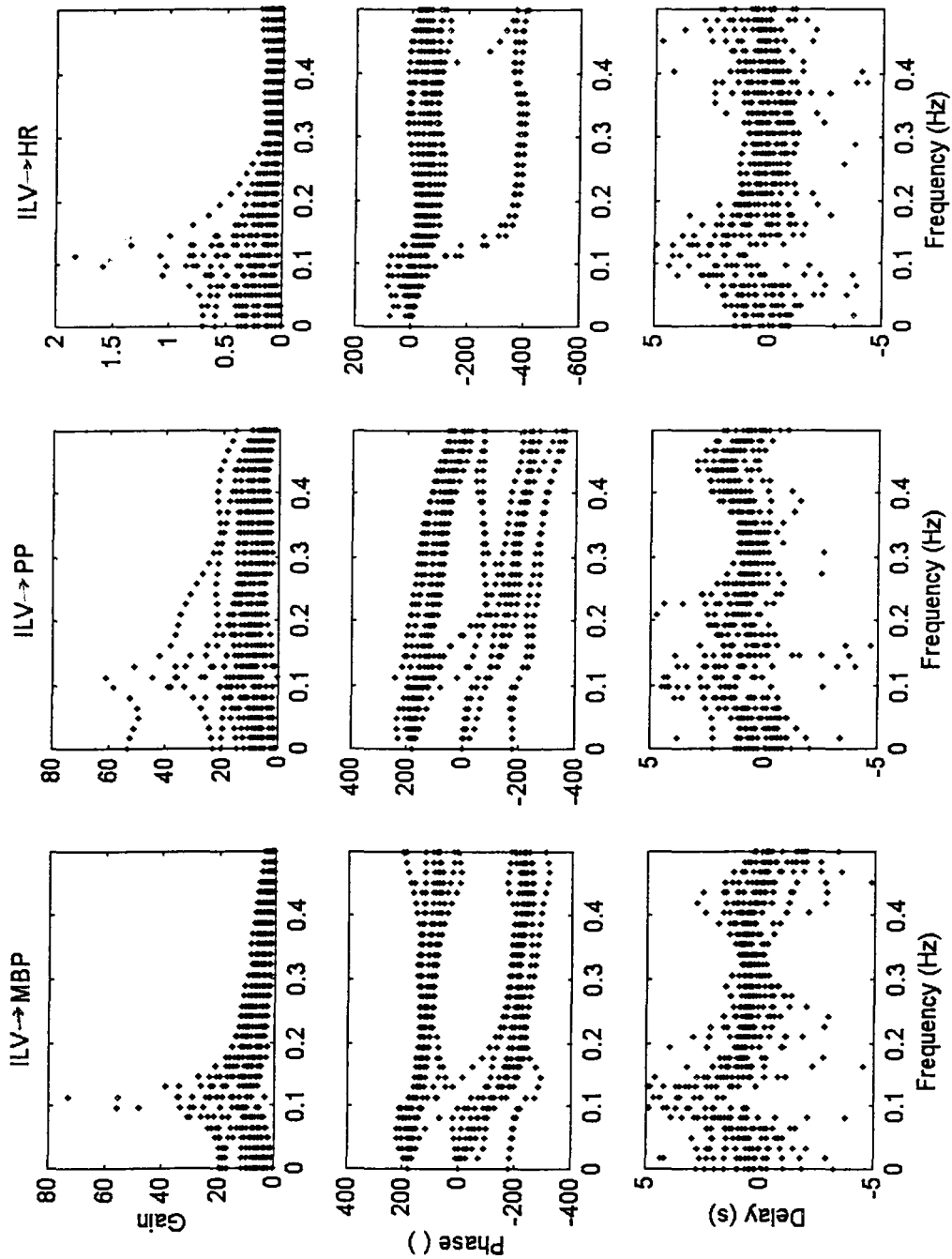
Figure 14: Group LSSM transfer functions for 10 subjects in the standing condition
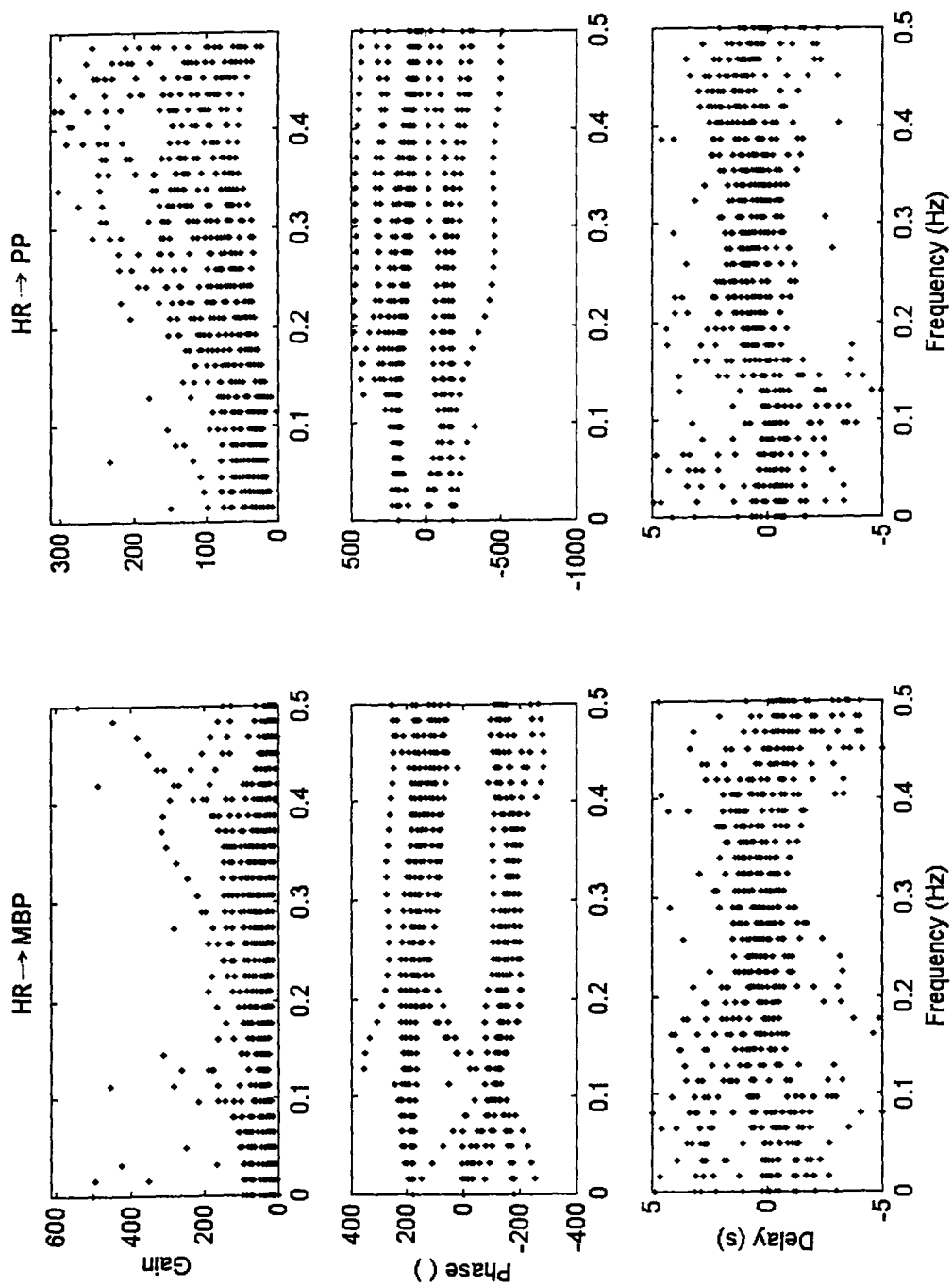
Figure 15: LSSM closed-loop transfer functions for 10 subjects in the standing condition.

3.5 Intra-Subject Variability

The standing condition transfer function results from a single subject using the three different ILV pacing waveforms as the input stimulus are shown in Figure 16. Intra-subject variability is significant, particularly in the magnitude function and at low frequencies. The phase functions and group delay functions are relatively reproducible if the spikes in the group delay functions are removed. Variability of the transfer function results reflects changing physiological conditions which may occur spontaneously over time or in response to the different ILV pacing functions patterns during the experiment.
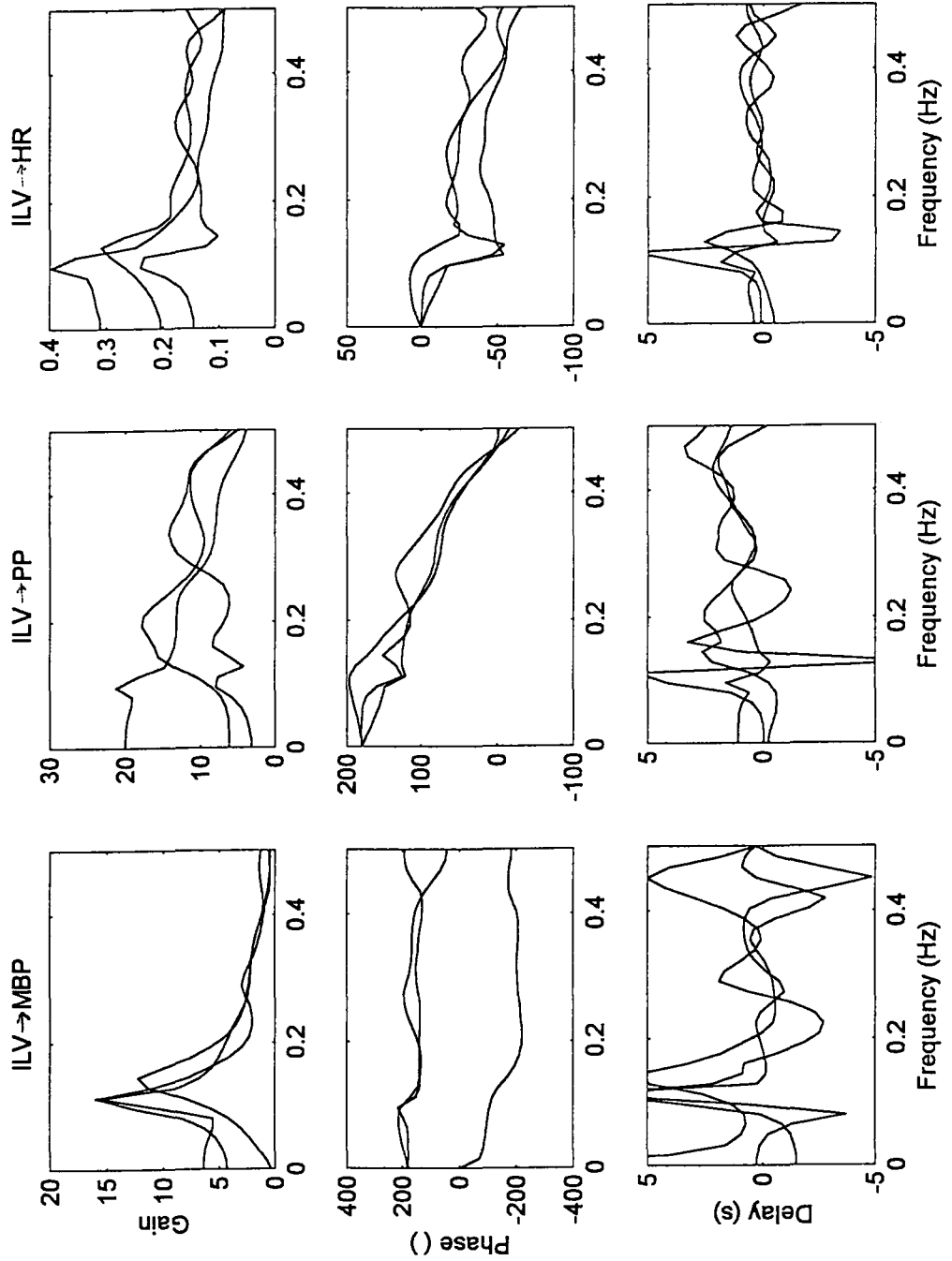
Figure 16: LSSM transfer functions from a single subject using the three different ILV pacing waveforms.

3.6 Causality of HR → PP

The zero-pole plots of the HR → PP transfer functions from nine of the subjects in the standing condition are shown in Figure 17. Most of the uncancelled poles and zeros are located inside the unit circle with a few located outside $|z| = 1$. Thus, neither the HR → PP nor the PP → HR transfer functions are strictly causal. This implies that changes in HR both cause and are caused by changes in PP, as expected. The presence of poles and zeros both inside and outside the unit circle indicates that some changes in PP are based on future values of HR and vice-versa. The means that PP and HR must share a common input (for example, ILV).
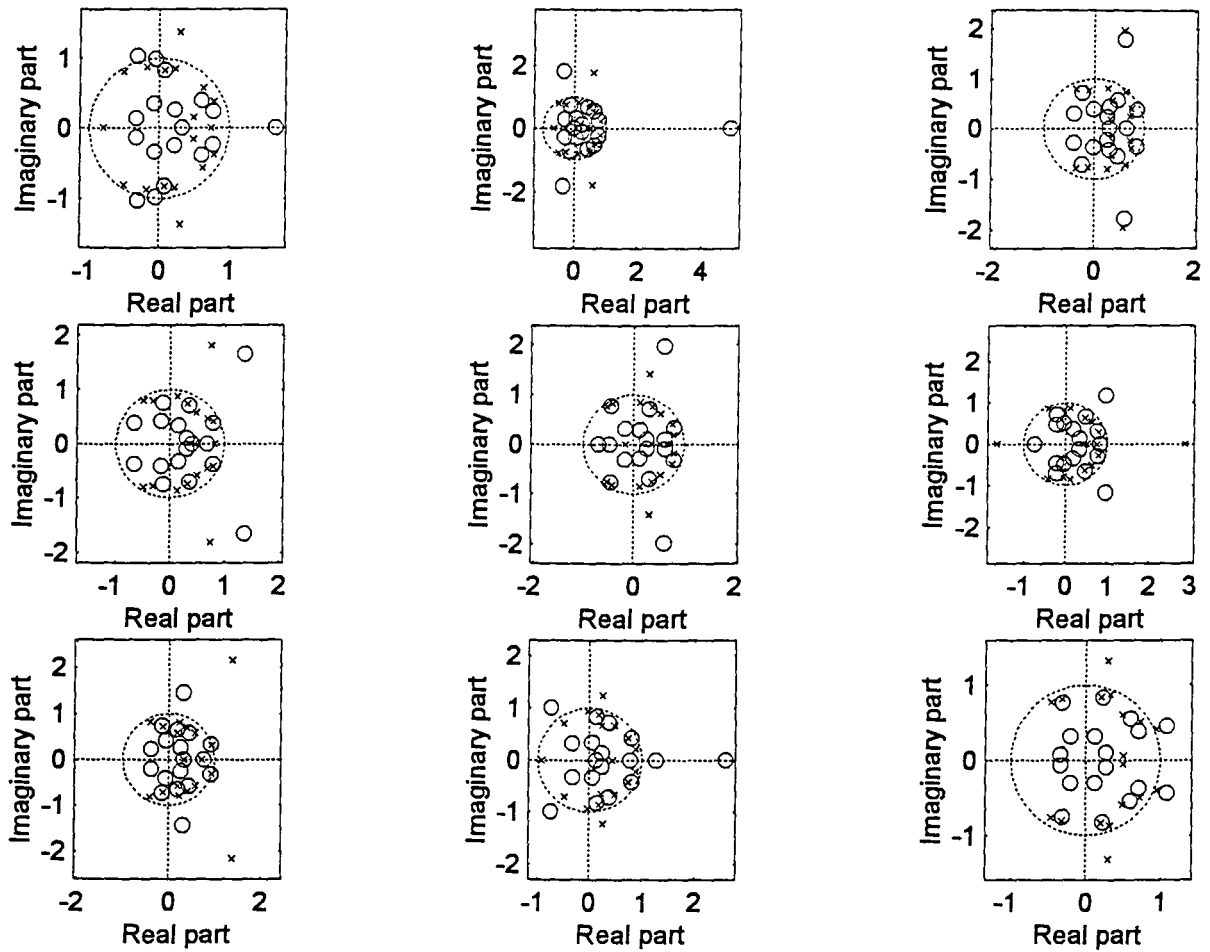
Figure 17: Pole-zero plots of the HR → PP transfer functions from 9 subjects in the standing condition. The poles ('x') and zeros ('o') are distributed both inside and outside the unit circle, so neither output is strictly causal with respect to the other.

Chapter 4: Discussion

4.1 Prediction Errors

The concentration of PE power at low frequencies has been observed previously with ARMA models of the system and by examination of cross-spectral coherence in non-parametric transfer function models. The PE observed in this work may be caused by an exogenous, non-observable system input and/or non-linear distortion of the ILV. Previous investigators have used non-linear generalized techniques (2nd order NARMA and Volterra kernels) to characterize the system more accurately [Marmarelis 1993, Chon 1996, Christini 1995]. They have found that the PE is moderately reduced but not eliminated with the introduction of nonlinearity into the system model. Thus, the most likely cause of the large PE in this work is an unobservable exogenous input to the system that results in large amplitude LF fluctuations in HR and BP. However, it is still possible that ILV may modulate this input of the system response in a non-linear fashion. Unfortunately, this possibility cannot be validated even using non-linear modelling techniques because the exogenous input is not directly observable.

The LF 'noise' in the system interferes with the LSSM modelling algorithm because the amplitude of the noise is usually larger than that of the signal. Thus, the first

N principal components of the data matrix include significant contributions from the LF noise. In this case, the LF power is implicitly modeled as an auto-regressive process in the outputs, where the unknown exogenous input is assumed to be Gaussian distributed white noise present in the ILV signal. This representation is obviously wrong and is responsible for the large group delay spikes at low frequency in the transfer function results.

One way to reduce the impact of the LF noise on the system model would be to reject the first M principal components of H, where $0 > M \ll N$, when reconstructing the state-vector sequence. However, doing so risks destroying the most important signal information as well, particularly if M is chosen too large or if the signal and noise power are roughly equal.

4.2 Comparison of LSSM Transfer Functions with Spectral Techniques

The magnitude function results are similar to those reported by other investigators using spectral methods [Berger 1989, Saul 1991], up to an arbitrary scaling constant which depends on the scaling of the input ILV signal. Where the magnitude functions differ, the coherence function of the spectral technique results is <0.5, indicating that the spectrally derived magnitude functions are not reliable in these regions. Of course, the LSSM transfer functions are also not reliable at LF, as evidence by relatively high PE in this frequency band and the tendency of the LSSM to model large amplitude LF noise as an AR process in the outputs.

The LSSM phase functions results generally agree with those found by previous investigators using spectral techniques [Saul 1991, Berger 1989]. The only significant difference appears in the ILV → PP and ILV → BP phase functions, for which Saul et al. obtain a -90° ± 20° net phase shift (after linear trend removal) whereas the LSSM yields ±180° ± 20° for these phase shifts. The reason for this difference is not known, although it may result from differing ways of preprocessing the input-output data.

Saul et al. [1991] also find smaller magnitude linear trends in the phase functions. However, the magnitude of the linear trend is sensitive to the temporal alignment of the ILV time series with the output time series during the modelling procedure and thus this difference may simply be an artifact of different synchronization methods.

4.3 Physiological Interpretation

The mean group delay and the stable regions of the group delay functions indicate that in the supine condition, changes in ILV cause changes in HR within 0.5 s, followed shortly (0.3 - 1 s) by changes in PP and finally changes in MBP 1 - 2 s later. These results support the hypothesis that the Bainbridge reflex plays a important role in the initial increase of HR during inspiration. The closed-loop transfer functions furthur reveal that the time lags associated with these responses are mostly caused by a fixed time lag between HR and PP of about 0.5 s or 1 heart beat.

In the standing condition, the changes in ILV effect HR sooner but the delay between HR and PP is unchanged. Thus, this is likely due to increased atrial stretching during inspiration while standing. The standing MBP response is also faster, which may be due to increased gravitational pooling of blood when standing. Gravitational pooling would cause systolic BP to drop faster after each heart beat and hence would lower the MBP more rapidly than when supine. This hypothesis is supported by the observation that the attenuation constant of the MBP magnitude function also increases upon standing, indicating that the increase in the MBP response is concentrated at low frequencies, or relatively slow changes like the diffusion of blood through capilliaries. Unfortunately, the magnitude function is not as reliable at low frequency as at higher frequencies because of the LF spikes introduced by the LSSM algorithm. Thus, the heightened MBP response at LF may also be an artifact of increased LF noise in MBP when standing.

The diminished PP and HR magnitude functions upon standing suggests that the coupling between respiratory activity and cardiovascular response is diminished when standing. This is in agreement with results from PS/HRV analysis of vagal tone during spontaneous breathing [Malik 1996]. The response may be due to any number of physiological changes associated with standing, including diminished venous return to the heart because of gravitational pooling of blood, reduction in baroreceptor and/or Bainbridge reflex responsiveness, altered breathing patterns, etc.

The causality analysis of the HR → PP zero-pole plots indicates that the HR → PP response is neither completely causal nor anti-causal, but rather a combination of the two.

Thus, both HR and PP are affected directly by ILV or some other common mechanisms related to respiration as well as through feedback paths. This supports the hypothesis that lung stretch receptors and/or direct input from the medulla may be partly responsible for generation of RSA.

For ILV inputs with power in primarily the 0.18 - 0.3Hz band one can approximate each of the output responses with the fixed delays and phase shifts in Table 1 because the group delay and phase functions are essentially constant over this frequency interval.

Table 1: Narrow Band Transfer Function Constants

	Supine			Standing		
	HR	**PP**	**MBP**	**HR**	**PP**	**MBP**
Delay (s)	0 ± 0.5	0.5 ± 0.5	1.5 ± 1	0 ± 0.5	0.5 ± 1	0.5 ± 1
Phase Shift (°)	-30 ± 50	190 ± 30	0 ± 30	-50 ± 60	190 ± 45	0 ± 30

These fixed values may be used to describe the temporal evolution of HR and PP with respect to a single ILV cycle during sinusoidal breathing at 0.25 Hz, as shown in Figure 13. Note that the presence of both non-zero phase shift and group delay parameters makes the net phase relationship between the outputs strongly dependent on breathing frequency.

Phase 1 - First Half of Inhalation

During the first half of the inspiratory cycle, negative intrathoracic pressure from respiratory motion activates stretch receptors in the right atrium while the increased pressure gradient increases venous return to the right atrium of the heart and lungs. The stretch receptors activate the Bainbridge reflex, which must initially compete with the effects of residual acetylcholine on the heart from a baroreceptor reflex carried over from the previous breath, described in Phase 4. Thus, the HR is initially slower than average during the first half of the inhalation and continues to decrease until the effects of the residual acetylcholine have dissipated and the Bainbridge reflex begins to dominate the HR response.

The PP is initially higher than average and continues to increase during the first half of inhalation. The two effects that likely contribute to this response are increased blood flow from the lungs carried over from the previous respiratory cycle and decreased HR from the previous baroreceptor response. Near the end of this phase, and the beginning of Phase 2, the increased PP begins to activate the carotid baroreceptors which then begin to compete with the Bainbridge reflex to decrease HR

Phase 2 - Second Half of Inhalation

During the second half of the inhalation the HR increases because of the dominance of the Bainbridge reflex response to atrial stretch. The increased HR decreases the diastolic filling time and hence the stoke volume. This causes the pulse pressure to level-off and begin to decrease during this phase of inspiration. Total cardiac output begins to rise at this time, despite the drop in stroke volume and PP. This causes the MBP to begin to rise as the arterial and venous pressure begin to adjust to the change in cardiac output.

Phase 3 - First Half of Exhalation

During the first half of exhalation, the baroreceptor reflex (activated in Phase 1 and 2) begins to overcome the Bainbridge reflex and decrease the HR. The PP begins to increase at this time from the combined effect of the decreasing HR (increasing diastolic filling time) and the increasing flow of oxygenated blood from the lungs.

Phase 4 - Second Half of Exhalation

During the final stage of exhalation, HR continues to decrease because of the baroreceptor reflex activated in Phase 1 and 2. The PP also continues to increase in response to lower HR (longer diastolic filling time) and increased blood flow from the lungs.
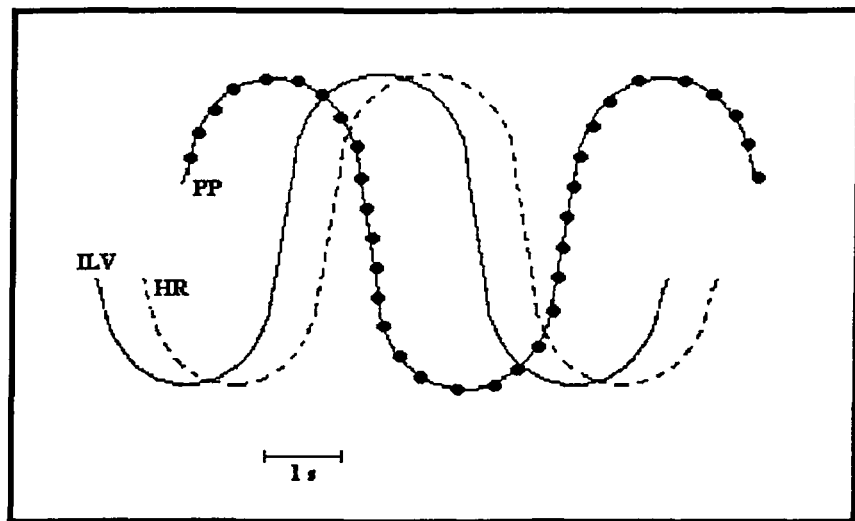
Figure 18: Phase relationships between ILV, HR, and PP based on the group transfer function results for a breathing rate of 0.25 Hz.

The above analysis is based on the assumption that the classical model for RSA generation is essentially correct. The contributions of lung stretch reflexes, chemoreceptor activation and central medullar influences are not included in this interpretation but may well play a role. Other interpretations of the transfer functions are certainly

possible. Nevertheless, the fact that the transfer function analysis results are not contrary to the expected (classical) behavior is reassuring.

4.4 Clinical Significance of Transfer Function Analysis

The transfer function analysis presented in this thesis may be of use in diagnosis of cardiorespiratory dysfunction. Until now, there has been no way to accurately determine the actual time delays embedded into the closed loop activity of the cardio-respiratory system. The results from this work show that the time delays (for example, the HR $\rightarrow$ PP delay) tend to be somewhat more stable with respect to changes in physiological condition (standing vs. supine) particularly in the 0.2 - 0.4 Hz band. This suggests that accurate estimation of time delays may be a more robust assessment of cardiovascular integrity than the more common used power spectral analysis of HR variability (PS/HRV). For example, a patient with an impaired Bainbridge reflex but no other physiological abnormalities might be expected to have slightly reduced power in the high frequency (HF) band of PS/HRV. However, the HF power is strongly dependent on autonomic arousal and physiological state [Malik 1996]. Thus, the correct diagnosis of low HF as a dysfunctional Bainbridge reflex would be unlikely because the specificity of the PS/HRV diagnosis is poor. By using transfer function analysis however, one would likely find an increased time delay between ILV and HR, reflecting the disabled Bainbridge response. According to the results from this work, this time delay would be relatively independent of

physiological state. Thus, the transfer function analysis could be used to make a more reliable diagnosis of certain physiological disorders.

4.5 Intra-Subject Variability

The variability of the transfer functions for the same subject may be caused by physiological changes between experiments and/or different physiological responses to the three different paced breathing series. The inherent variability has been observed in PS/HRV experiments which show that vagal tone varies significantly even under stationary conditions [Bianchi 1997, Kamath 1993]. Relatively large intra-subject variability indicates that the transfer function analysis technique is highly sensitive to physiological changes. However, the transfer functions are not generally reducible to specific physiological changes, so the specificity of the technique is relatively poor.

Chapter 5: Limitations

5.1 Linearity

The LSSM technique as developed in this thesis is suitable only for linear systems. If the system is strongly non-linear or has both linear and non-linear components then the technique will fail to capture the system dynamics. Unfortunately, the parameters from non-linear system modelling techniques are not easily related to the underlying physiology, unless the non-linearities are chosen based on known physiological mechanisms. Thus, extending the LSSM algorithm to include generalized non-linear behavior would not be productive.

5.2 Stationarity

The LSSM technique developed in this thesis assumes that the system being modelled is stationary over the input-output data set. Although the amount of data required by the LSSM is less than with other techniques the amount is still significant. One effect of non-stationarity on the LSSM model is that the estimated system order

(based on the SVD of the input-output data) will be surprisingly large and the model will still not perform well.

5.3 Effects of Exogenous Unknown Inputs

The LSSM technique is well suited for linear system modelling with fairly high levels of background noise. However, if the system 'noise' is actually caused by an exogenous input that has a large effect on the outputs, then the LSSM method will fail because it will erroneously model the noise as an AR process that is excited by noise in the input.

5.4 Non-Sinusoidal Breathing Patterns

Transfer function results are difficult to interpret in the time domain when the input function is not near-sinusoidal. This complicates the interpretation of the LSSM results in terms of physiology because normal breathing patterns are never sinusoidal. One way to overcome this technical difficulty may be to transform the transfer functions using a set of normalized respiration wavelets as an alternative basis set to the complex exponentials. In this case, the frequency axis of the transfer functions could refer to time dilated respiration wavelets rather than sinusoids.

5.5 Non-Physiological Experimental Conditions

The transfer functions developed in this thesis require controlled respiration to enforce causality on the system outputs and to ensure that all the system states are persistently excited for reliable identification of the parameters. Unfortunately, respiration is normally connected in feedback with the other components of cardiovascular regulation. The true inputs to the system are numerous and generally not observable. Thus, the transfer functions developed using paced respiration are not entirely representative of normal cardio-vascular regulation.

The interpolated time series results also show that controlled breathing has a marked effect on physiological state, causing drowsiness and sometimes reduced blood pressure over the course of the controlled breathing experiment. The consequences of these physiological changes on the 'true' transfer function results are difficult to quantify.

5.6 Temporal Uncertainty in the Input-Output Data

Representation of HR and BP discrete event series as a discrete time series limits the temporal resolution of any analysis method, independent of sampling rate. This is because the time series must be interpolated from the HR and BP point series and interpolation assumes that the time series changes in a predictable way in between the 'known' points of the event series. Thus, the temporal uncertainty of the HR and BP time

series is limited to about half a heart beat or 0.5 s. This uncertainty is inherent in the HR and BP event series and cannot be corrected or eliminated. The temporal resolution of the time series limits the physiological reliability of the group delay function for comparing small changes in time delays between the system outputs.

Another source of temporal uncertainty is introduced during the alignment of the continuous time ILV series and the interpolated HR and BP series. To align the time series, one must arbitrarily decide if the first HR time series value corresponds to the first or to the second R-wave in the ECG and hence the start and end times of the ILV series. Since interpolation of HR and BP is a non-causal process which depends on both past and future R-R intervals, neither alignment is strictly correct. The uncertainty in this alignment is about one R-R interval and affects the HR and BP results identically as a constant delay or time advance of the system input with respect to the outputs.

The alignment uncertainty is generally independent from the interpolation uncertainty. Thus, the total temporal uncertainty in the group delay function is approximately 0.7 - 1.5 s. Note that this uncertainty refers to the physiological interpretation of the group delay results and not to the LSSM group delay function itself. However, the temporal uncertainty may be one reason why the inter-subject and intra-subject group delay variability is high.

5.7 Reliability of Closed-Loop Transfer Functions

Interpretation of the closed-loop system responses is limited by the reliability of the close-loop system transfer functions. Specifically, if the zeros of the zeros of the LSSM transfer functions are not entirely reliable, then the closed-loop magnitude functions will be affected by problems with numerical instability from partial pole-zero cancellations where there should be total cancellation. One way to circumvent this problem may be to manually delete pole and zeros that "nearly" cancel from the numerators of $G(z)$ prior to computing the closed loop transfer functions.

More importantly, it can be shown that the closed-loop identifiability of a system is not guaranteed, even when the system inputs are persistently exciting [Ljung, 1987]. Unfortunately, the LSSM may still perform well, as judged by the simulation results on validation data, even if the input-output data does not contain enough information to uniquely determine the output-output transfer functions. Thus, it may be very difficult to decide if the closed-loop transfer functions are reliable.

Chapter 6: Conclusions

Closed-loop analysis of cardiovascular regulation was reexamined and improved using state-space modelling techniques. Physiological interpretation of the system transfer functions was facilitated by the theoretical development and application of group delay and causality analysis in SIMO systems. The new techniques allow one to infer physiologically relevant time delays from analysis of input-output data and describes a causality relationship between the system outputs, if such a relationship exists. The results of the analysis on ten healthy human subjects generally supports the classical model hypothesis for the generation of RSA in humans and extend the model to include measurable time delays for BP and HR responses to ILV.

Appendix A: LSSM Algorithm in MATLAB

```
function [A,B,C,D]=LSSM(u,y,R)
% Linear State-Space Modelling (LSSM) algorithm
% adapted from: Moonen, M. Int. J. Control. Vol. 49 No. 1 p. 219-232, 1989
% c. Andrew May 1998.
% The only changes from the paper are in terminology as follows:
% (i) "x" is the dimension of the state space (not "n")
% (ii) "n" is the number of outputs (not "l")
% (iii) "TR" and "TL" are temporary matrices only (not in the paper at all)
% Arguments:
% u,y input and output data matrices with the data organized in rows
% with the first sample of the data corresponding to the first column.
% R = matrix rectangularity (ratio of # columns to # block rows).
% Outputs:
% matrices A,B,C,D in the LSSM equations:
% x(k+1)=Ax(k) + bu(k) and  y(k)=Cx(k)+Du(k)
%This is a prediction error model where measurement and state noise
% are not explicitly modelled and hence contribute to the model prediction errors.
m=size(u,1); % number of inputs
n=size(y,1); % number of outputs
Rmin=max(m,n)*R; % true rectangularity of the joint data matrix H
N=length(u);
j=fix(Rmin*N/(1+Rmin)); % number of columns in H
% j >> max(m,n)*number of block rows in H [Moonen 1989]
H=[];Uh=[]; %initialize input-output and input Hankel data matrices
for k=1:N-j+1
    H=[H;u(:,k:k+j-1);y(:,k:k+j-1)];     %fill the rest of the matrix up row by row
    Uh=[Uh;u(:,k:k+j-1)];
end
I=size(H,1); %total number of rows in H
i=fix(I/(m+n)/2); %1/2 the number of block rows in H
% minimum resolvable frequency of the LSSM
% is proportional to the length of the rows in H
%The number of columns in H is the length of the rows.
[V,S,U]=svd(H',0); %perform SVD of data matrix H (economy size)
                % H is the concatenation of H1 and H1 in [Moonen 1989]
S=S';
% Note: the parameter order in above SVD is reversed
% and the arguments are transposed.
```

% This is done to utilize the 'economy size'
% SVD routine in MATLAB. ie. if H=U*S*V' then H'=V*S'*U'.
% This is required since the economy size SVD only works if #rows>#cols in H.
% Perform SVD on input data matrix and compare singular value distributions
S_u=svd(Uh);
figure;
plot(diag(S),'b-')
hold on
plot(S_u,'r-');
zoom on
legend('input AND output data','input data');
title('Singular Value Distributions');
x=input(['   Please estimate the system order (maximum = ',int2str(n*i-1),'): ']);
% The system order is limited because this algorithm computes a basis for 1/2
% of the state-space realization using all of the data. Although it limits
% the realizable system order, the method is less sensitive to noise
% and round-off error. It essentially assumes that the basis for the state-space
% does not change from the 1st half to the 2nd half of the input-output data.
% (i.e. that the system is stationary and sufficiently excited by the input sequence
% so that all modes of the system are expressed in both sections of the input-
% output data.
U11=U(1:(m*i+n*i),1:2*m*i+x);
% sub-matrices extracted U to increase computational efficiency
U12=U(1:(m*i+n*i),1:2*n*i-x);
S11=S(1:2*m*i+x,1:2*m*i+x);
[Vq,Sq,Uq]=svd((U12'*U11*S11)',0);
%same "economy size" SVD as before
Uq=Uq(1:(2*n*i-x),1:x);
% Use the 1st "x" principal components of the SVD
% (ie. the 1st "x" columns of Uq) as a basis for X2 [Moonen 1989]
TL=[Uq'*U12'*U(m+n+1:(i+1)*(m+n),:)*S;U(m*i+n*i+m+1:(m+n)*(i+1),:)*S];
TR=[Uq'*U12'*U(1:m*i+n*i,:)*S;U(m*i+n*i+1:m*i+n*i+m,:)*S];
ABCD=TL*pinv(TR); %mean square solution of the above equation
%solve TL=ABCD*TR for ABCD
[Rows,Cols]=size(ABCD);
A=ABCD(1:Rows-n,1:Cols-m);
B=ABCD(1:Rows-n,Cols-m+1:Cols);
C=ABCD(Rows-n+1:Rows,1:Cols-m);
D=ABCD(Rows-n+1:Rows,Cols-m+1:Cols);
% Segment ABCD state space matrix into A,B,C, and D
% where u,y,x are all column "vectors"
% (or block column matrices for MIMO systems).

Appendix B: Closed Loop Transfer Functions

In this section I derive the relationship between the global and closed-loop transfer functions of the LSSM for a one-input two-output system. However, the results may be extended to include any SIMO system through an analogous analysis.

Consider the SIMO system shown in Figure 19
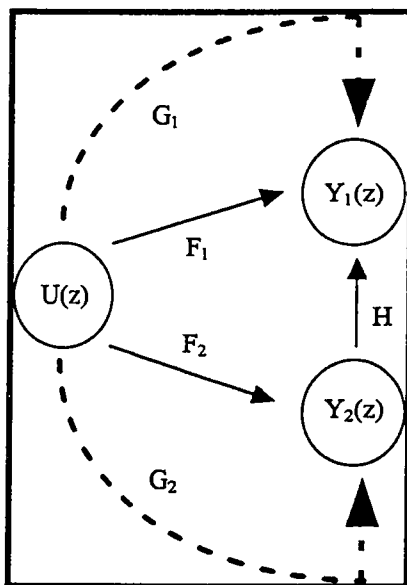
Figure 19: Schematic diagram of a single-input two-output system.

Here, G_1 and G_2 are the "global" causal transfer functions from $U(z)$ to $Y(z)$ which are derived from the LSSM parameters and (12). The goal of this analysis is to

extract the closed-loop transfer functions F_1, F_2 and H from G_1 and G_2. The two

equations relating the closed-loop to global transfer functions may be written by inspection

$$G_1 = F_1 + F_2 H$$
$$G_2 = F_2 + F_1 H^{-1}$$
(B1)

Since G_1 and G_2 are the rows of the transfer function matrix in (12) the two global

transfer functions have a common denominator polynomial ($|zI-A|$). The right side of (B1)

can be expressed in terms of this common denominator

$$G_1 = \frac{num(H)[num(F_1)den(F_2)den(H) + num(F_2)num(H)den(F_1)]}{den(F_1)den(F_2)den(H)num(H)}$$
(B2)
$$G_2 = \frac{den(H)[num(F_2)den(F_1)num(H) + num(F_1)den(H)den(F_2)]}{den(F_1)den(F_2)den(H)num(H)}$$

where num($\bullet$) and den($\bullet$) are numerator and denominator polynomials respectively. This

allows one to solve for H directly from the ratio of G_1 to G_2

$$\frac{G1}{G2} = \frac{num(H)}{den(H)} = H$$
(B3)

It is important to realize that the existence of H is an assumption which cannot be

derived from the input-output data alone. Furthermore, if H is assumed to exist, then F_1

and F_2 are not uniquely identifiable. Conversely, if H is assumed not to exist, then F_1 and

F_2 are unique and equal to G_1 and G_2 respectively.

The complete identifiably of **H** requires specification of an appropriate ROC as well as the location of the poles and zeros of **H**. Again, the selection of the ROC, if it is not unique, is an assumption that cannot be validated by the information in the input-output data. These limitations are inherent in the identification of closed-loop systems from input-output data. The advantage of the LSSM technique over specialized ARMA models is that the assumptions need not be made until after the model parameters are fit and the transfer functions are to be interpreted.

In the case where the number of inputs is greater than two, the above analysis holds only if all the system outputs are interdependent (i.e. all of the **H** functions exist). If this is not the case, then the equations must be rederived appropriately and may not have a unique solution.

BIBLIOGRAPHY

Banerjee, P. Shah, S.L. "Simultaneous Estimation of Parameters for Different Orders of Discrete Orthonormal Function Models", IEEE Trans. Sig. Proc. Vol 44, No 8, . Aug. 1996.

Berger, R.D. Saul, J.P. Cohen, R.J. "Assessment of Autonomic Response by Broadband Respiration". IEEE Trans. Biomed. Eng, Vol 36, No 11, pp 1061-1064, Nov 1989.

Bernardi, L. Keller, F. Sanders, M. Reddy, P.S. Griffith, B. Meno, F. Pinsky, M.R. "Respiratory Sinus Arrhythmia in the Denervated Human Heart", J. Appl. Physiol. Vol 67, No 4, pp 1447-1455, 1989.

Bernardi, L. Salvucci, F. Suardi, R. Soldá, P.L., Calciati, A. Perlini, S. Falcone, C. Ricciardi, L. "Evidence for an Intrinsic Mechanism Regulating Heart Rate Variability in the Transplanted and Intact Heart During Submaximal Dynamic Exercise?", Cardiovascular Research, Vol 24, pp 969-981, 1990.

Berne, R. Levy, M. Principles of Physiology. St. Louis: CV Mosby Company, 1990, Ch 2,4-5.

Bianchi, A.M. Mainardi, L.T. Meloni, C. Chierchia, S. Cerutti, S. "Continuous Monitoring of the Sympatho-Vagal Balance Through Spectral Analysis", IEEE Eng. Med Bio. pp 64-73, Sept./Oct. 1997.

Casadel, B. Meyer, T.E. Coats, J.S. Conway J. Sleight, P. "Baroreflex Control of Stroke Volume in Man: An Effect Mediated by the Vagus", J. Physiol., Col 448, pp 539-550, 1992.

Chon, K.H. Mukkamala, R.Toska, K. Mullen, T.J. Armoundas, A.A. Cohen, R.J. "Linear and Nonlinear System Identification of Autonomic Heart-Rate Modulation", IEEE Eng. Med. Bio, pp 96-105, Sept/Oct 1997.

Chon, K.H. Mullen, T.J. "A Dual-Input Nonlinear System Analysis of Autonomic Modulation of Heart Rate", IEEE Trans. Biomed. Eng. Vol 43, No 5, May 1996.

Christini, D.J. Bennett, F.M. Lutchen, K.R. Ahmed H.M. Hausdorff, J.M. Oriol, N. "Application of Linear and Nonlinear Time Series Modelling to Heart Rate Dynamics Analysis", IEEE Trans. Biomed. Eng. Vol 42, No 4, Apr. 1995.

De Boer, R.W. Karemaker, J.M. "Relationships Between Short-Term Blood-Pressure Fluctuations and Heart-Rate Variability in Resting Subjects II: A Simple Model", Med. Biol. Eng. Comput. Vol 23, 1985.

DeBoer, R.W. Karemaker, J.M. Strackee, J. "Hemodynamic Fluctuations and Baroreflex Sensitivity in Humans: a Beat-to-Beat Model", Am. J. Physiol. Vol 253, pp 680-689, 1987.

Freyschuss, U. Melcher, A. "Sinus Arrhythmia in Man: Influence of Tidal Volume and Oesophageal Pressure", Scand. J. Clin. Lab. Invest. Vol 35, pp 487-496, 1975.

Golub, G.H. Van Loan, C.F. Matrix Computations. Baltimore: Johns Hopkins University Press, 1996.

Haykin, S. Adaptive Filter Theory (3rd Ed.). New Jersey: Prentice Hall, 1996.

Haykin, S. An Introduction to Analog and Digital Communications. New York: John Wiley and Sons, 1989.

Jose, A. "Effect of Combined Sympathetic and Parasympathetic Blockade on Heart Rate and Cardiac Function in Man", Am. J. Cardiology, Vol 18, pp 476-478, Sept. 1966.

Kailath, T. Linear Systems. New Jersey: Prentice-Hall, 1980.

Kamath, M.V. Fallen, E.L. "Power Spectral Analysis of Heart Rate Variability: A Noninvasive Signature of Cardiac Autonomic Function", Crit. Rev. Biomed. Eng., Vol 21 No. 3, pp 245-311, 1993.

Ljung, Lennart. System Identification: Theory for the User. New Jersey: Prentice-Hall, 1987.

Lown, B. Malliani, A. Prosdocimi, M. Neural Mechanisms and Cardiovascular Disease. Fidea Research Series, Vol 5, Padova: Liviana Press, 1986.

Malik, M. "Standards of Heart Rate Variability", Circulation, Vol 93, No 5, pp 1052-1064, Mar 1996.

Malliani, A. "Cardiovascular Sympathetic Afferent Fibers", Rev. Physiol. Biochem. Pharmacol. Vol 94, pp 11-66, 1992.

Marmarelis, V.Z. "Identification of Nonlinear Biological Systems Using Laguerre Expansions of Kernels", Annals Biomed. Eng. Vol 21, pp 573-589, 1993.

Moonen, M. De Moor, B. Vandenberghe, L. Vandewalle, J. "On-Line and Off-Line Identification of Linear State Space Models", Int. J. Cont, Vol 49, No 1, pp 219-232, 1989.

Moonen, M. Ramos, J. "A Subspace Algorithm for Balanced State Space System Identification", IEEE Trans. Auto. Control, Vol. 38, No 11, pp 1727-1729, Nov. 1993.

Mullen, T.J. Appel, M.L. Mukkamala, R. Mathias, J.M. Cohen, R.C. "System Indentification of Closed-Loop Cardiovascular Control: Effects of Posture and Autonomic Blockade", Am. J. Physiol. Vol 272, pp H448-461, 1997.

Novak, V. Novak P. De Champlain, J. Le Blanc, A.R. Martin R. Nadeau, R. "Influence of Respiration on Heart Rate and Blood Pressure Fluctuations", J. Appl. Physiol., Vol 17, No 2, pp 617-626, 1993.

Oppenheim A. Discrete-Time Signal Processing. New Jersey: Prentice Hall, 1989.

Passino, C. Slight, P. Valle, F. Spadacini, G. Leuzzi, S. Bernardi, L. "Lack of Peripheral Modulation of Cardiovascular Central Oscillatory Autonomic Activity During Apnea in Humans", Am Phys. Soc., pp H123-129, 1997.

Perrott, M.H. Cohen, R.J. "An Efficient Approach to ARMA Modelling of Biological Systems with Multiple Inputs and Delays", IEEE Trans. Biomed. Eng. Vol 43, No 1, Jan. 1996.

Piepoli, M. Slight, P. Leuzzi, S. Valle, F. Spadacini, G. Passino, C. Johnston, J. Bernardi, L. "Origin of Respiratory Sinus Arrhythmia in Conscious Humans", Circulation, Vol. 95, No. 7, April 1997.

Sanders, J.S. Ferguson, D.W. Mark, A.L. "Arterial Baroreflex Control of Sympathetic Nerve Activity During Elevation of Blood Pressure in Normal Man: Dominance of Aortic Baroreflexes", Circulation, Vol 77, No 2, pp 279-288, 1988.

Saul, J. Berger, R.D. Albrecht, P. Stein, S.P. Chen, M.H. Cohen, R.J. "Transfer Function Analysis of the Circulation: Unique Insights into Cardiovascular Regulation", Am. J. Physiol., Vol 261, pp H1231-1245, 1991.

Seals, D. Suwarno, N.O. Joyner, M.J. Iber, C. Copeland, Dempsey, J.A. "Respiratory Modulation of Muscle Sympathetic Nerve Activity in Intact and Lung Denervated Humans", Circulation Research, Vol 72, pp 440-454, 1993.

Signal Processing Toolbox User's Guide. Math Works Inc, 1996.

Sinha, N.K. Kuszta, B. Modelling and Identification of Dynamic Systems. New York: Van Nostrand Reinhold Co, 1983.

Strang, G. Linear Algebra and its Applications. New York: Academic Press, 1980.

Sleight, P. La Rovere, M.R. Mortara, A. Pinna G. Maestri, R. Leuzzi, S. Bianchini, B. Tavazzi, L. Bernardi, L. "Physiology and Pathophysiology of Heart Rate and Blood Pressure Variability in Humans: is Power Spectral Analysis Largely an Index of Baroreflex Gain?", Clinical Science, Vol 88, pp 103-109, 1995.

Taha, B.H. Simon, P.M. Dempsey, J.A. Skatrud, J.B. Iber, C. "Respiratory Sinus Arrhythmia in humans: an Obligatory Role for Vagal Feedback from the Lungs", J. Appl. Physiol. Vol 78, No 2, pp 638-645, 1995.

Taylor, J.A. Eckberg, D.L. "Fundamental Relations Between Short Term RR Interval and Arterial Pressure Oscillations in Humans", Circulation, Col 93, pp 1527-1532, 1996.

Triedman, J.K. Saul, J.P. "Blood Pressure Modulation by Central Venous Pressure and Respiration: Buffering Effects of the Heart Rate Reflexes", Circulation Vol 89, pp 169-179, 1994.

Woo, K.S. Bernardi, L. "Impact of Changes in Respiratory Frequency and Posture on Power Spectral Analysis of Heart Rate and Systolic Blood Pressure Variability in Normal Subjects and Patients with Heart Failure.", Clinical Science, Vol. 91, pp 35-43, 1996.

Van de Vegte, J. Feedback Control Systems, 2nd ed. New Jersey: Prentice-Hall, 1990.